

Dynamic Instabilities in Slender Space Launch Vehicles under Propulsive Thrust and Aerodynamic Forces

M. Trikha¹, S. Gopalakrishnan², D. Roy Mahapatra²
R. Pandiyan¹

Abstract: A mechanics based linear analysis of the problem of dynamic instabilities in slender space launch vehicles is undertaken. The flexible body dynamics of the moving vehicle is studied in an inertial frame of reference, including velocity induced curvature effects, which have not been considered so far in the published literature. Coupling among the rigid-body modes, the longitudinal vibrational modes and the transverse vibrational modes due to asymmetric lifting-body cross-section are considered. The model also incorporates the effects of aerodynamic forces and the propulsive thrust of the vehicle. The effects of the coupling between the combustion process (mass variation, developed thrust etc.) and the variables involved in the flexible body dynamics (displacements and velocities) are clearly brought out. The model is one-dimensional, and it can be employed to idealised slender vehicles with complex shapes. Computer simulations are carried out using a standard eigenvalue problem within h - p finite element modelling framework. Stability regimes for a vehicle subjected to propulsive thrust are validated by comparing the results from published literature. Numerical simulations are carried out for a representative vehicle to determine the instability regimes with vehicle speed and propulsive thrust as the parameters. The phenomena of static instability (divergence) and dynamic instability (flutter) are observed. The results at low Mach number match closely with the results obtained from previous models published in the literature.

Keywords: launch vehicle, stability, flexible body, follower force, aerodynamic forces, propulsive thrust.

1 Introduction

Stability is an important issue in the design and performance analysis of space launch vehicles. This issue is becoming increasingly important as various ways

¹ ISRO Satellite Centre, Indian Space Research Organization, Bangalore 560017, India

² Department of Aerospace Engineering, Indian Institute of Science, Bangalore 560012, India

and options in space flight (including hypersonic flight) are taking shape. There are various sources of instabilities in this context (Himmelblau, Manning, Piersol & Rubin 2001). Instability in space vehicles may arise due to static and/or dynamic compressive loads resulting in structural buckling. Among other major factors affecting the stability is the varying flight regimes from transonic to supersonic and to hypersonic, due to which instability may occur at certain Mach numbers (NASA SP-8003, 1964). This may pose a severe problem for the structural integrity. Instabilities in space vehicles due to combustion process in solid rocket motors have been observed (Fabignon *et al.* 2003). Instabilities due to Pogo oscillations in liquid fueled rockets is another concern (Oppenheim & Rubin 1993). Any mechanical system subjected to impulsive loading, such as shock, may undergo instability (Ivanov 2001). In the context of perception of a hazard to the structural integrity, the effect of the impulsive nature of the structural change has a special significance. One of the tragic example of this is the failure of the space shuttle Challenger, where the failure was attributed to 'aerodynamic and inertia forces' or 'deflagration'. These were analysed in details by Jones & Wierzbicki (1987). Also, determining the role of damping on instability is critical for a non-conservative system (Bolotin, Grishko & Panov 2002). All of these aspects must be considered with great care, in the future space launch vehicle technology development.

Space launch vehicles can be treated under a broader perspective of axially moving structures. This is a classical problem. An extensive literature review of axially moving structures was carried out by Wickert & Mote Jr. (1988). The class of axially moving continua encompasses diverse mechanical systems, such as high speed magnetic and paper tapes, high speed band saw, paper webs, films, wide moving bands and belts etc. Wickert & Mote Jr. (1990) studied the classical vibration analysis of axially moving continua using a canonical state space form. Lin (1997) investigated the stability and vibration characteristics of axially moving plates. The transition from stable to unstable regime may occur in two different ways - divergence (static instability) and flutter (dynamic instability).

In aeronautical engineering applications, the terms divergence and flutter originated specifically during the investigation of sudden airplane blow-ups during 1910-1930 (Hodges & Pierce 2002). Hence, divergence and flutter are normally used in the context of problems of aeroelasticity observed in aircrafts, missiles and launch vehicles. Also, aeroelastic divergence of unguided launch vehicles, leading to structural failure has been reported by Young (1968). The observed phenomenon of flutter oscillations is in reality a nonlinear one (Dugundji 1992). But a linear theory often suffices in the prediction of the onset of flutter instabilities. However, if one is interested in the magnitude of flutter oscillations, nonlinear theory must be applied. Nonlinearities in aeroelasticity can arise from the structure or from the

aerodynamics (Dugundji 1992). The nonlinearities due to structure can be either geometrical or material. Geometrical nonlinearity can be due to large amplitude deflections of beams and panels and due to nonlinear behavior of joints and control systems. Material nonlinearity, due to nonlinear material behavior, results in nonlinear stiffness and damping characteristics. From the aerodynamics point of view, the nonlinearities can arise due to high angle of attack, resulting in flow separation. Nonlinearities can also arise from the transonic speed regime, where the flow equations are inherently nonlinear.

A number of researchers have studied the dynamic characteristics and stability of slender space launch vehicles. Meirovitch & Wesley (1967) studied the dynamic characteristics of a variable mass slender elastic body under high accelerations. They used a variational principle to obtain the coupled differential equations for rigid body and elastic motions. Beal (1965) studied the dynamic stability of a flexible missile under constant and pulsating thrusts and showed that the critical thrust magnitude, in the absence of control system, is associated with coalescence of the lowest two bending frequencies. Wu (1975, 1976) examined the stability of a free-free beam under axial thrust, subjected to directional control, using a finite element approach. Wu had stated that for a uniform free-free beam under a constant thrust, without directional control, there is only one zero eigenvalue corresponding to a rigid body translation. For a non-zero thrust, the eigenvalue corresponding to rigid body rotation, takes a positive real value and the unstable mode of disturbance is a bending mode. Sundararamaiah and Johns (1976) commented on Wu's papers that his results regarding the eigenvalue corresponding to rigid body rotation, taking a positive real value, are not correct due to error in one of the matrix terms. Park and Mote Jr. (1985) studied the problem of maximizing the controlled follower force on a free-free beam carrying a concentrated mass.

Bisplinghoff and Ashley (1962) studied the aeroelastic stability of one-dimensional slender vehicle configurations. Ericsson (1967) studied the problem of aeroelastic instability caused by slender payloads. Two flow states may exist on a launch vehicle payload fairing during transonic flight. The flow at the cone cylinder junction may be separated or attached. Ericsson and Reding (1986) investigated the flow separation phenomenon for launch vehicles with associated unsteady fluid mechanics. Humbad (1978) carried out static aeroelastic analysis of guided slender launch vehicles. Elyada (1989) developed a closed form approach to determine aeroelastic divergence in rocket vehicles. Dotson et al. (1998) studied the self sustained oscillation of a launch vehicle, from aeroelastic coupling. A dynamic aeroelastic analysis was performed by Ericsson and Pavish (2000) to calculate modal damping for proposed launch vehicles. Murphy & Mermagen (2003) employed aerodynamic and elastic symmetries to take advantage of the complex variable approach

to describe the flight motion of a continuously elastic finned missile. A linearized aeroelastic analysis for a launch vehicle in transonic flow conditions was carried out by Capri et al. (2006) considering unsteady flow. Problems of instability are observed in other diverse applications also. The phenomenon of divergence instability in the blade of a horizontal-axis wind power turbine was studied by Lin, Lee and Lin (2008). Flutter analysis of thermally buckled composite sandwich plates under aerodynamic pressure was carried out by Shiau and Kuo (2007). Stability analysis of beams rotating on an elastic ring with application to turbo machinery rotor-stator contacts was carried out by Lesaffre, Sinou and Thouverez (2007).

Propulsive thrust of a launch vehicle/ missile acts as a follower force. An extensive literature review of follower forces was carried out by Elishakoff (2005). Follower force comes under the category of non-conservative forces. Applied forces are said to be non-conservative if the work done by them is path dependent. Some non-conservative problems of elastic stability, especially those due to follower forces and aerodynamic forces, have been studied extensively by Bolotin (1963). In the published literature, flexible body dynamics of vehicles have been studied with respect to a body-fixed coordinate system, and the total derivatives of displacements in inertial axis have been neglected.

Various approaches can be utilized for modeling a space launch vehicle. Different computer modeling approaches in engineering can be found in reference (Atluri 2005). Two of the approaches that can be employed for modeling are the time Fourier Spectral Finite Element method and the h-p Finite Element method. The main task is to discretize the structure into finite elements for both the methods. The time-frequency Fourier spectral FEM (SFEM) developed by Doyle (1997), is ideally suited for analysing systems subjected to impact and shock loads which have very high frequency content. A matrix methodology was used for spectral analysis of wave propagation in multiple connected Timoshenko beams by Gopalakrishnan, Martin & Doyle (1992). A spectral finite element was formulated for a rotating beam subjected to small duration impact by Vinod, Gopalakrishnan and Ganguli (2006). Wave propagation analysis in isotropic plates was carried out by Mitra & Gopalakrishnan (2006) using wavelet based 2-D spectral finite element. In the present work, a space launch vehicle is modelled using beam finite elements within h-p finite element modeling framework. Finite element models with beam elements have been used previously for preliminary design of launch vehicles (Rainey 2004). These models are found to be quite adequate in assessing the dynamic characteristics of the vehicle.

A space launch vehicle undergoes large rigid body displacements, but a small strain assumption is appropriate for most of the flight conditions, except structural failure scenarios. If the instabilities occur, the elastic deformations grow with time

and hence non-linearities due to large deformation need to be considered. Several researchers have studied the dynamics of flexible structures undergoing large displacements and rotations. Kane and Levinson (1981) carried out simulation of large motions of spacecraft in orbit, modeled as a non-uniform unrestrained beam. Simo and Vu-Quoc (1988) developed a geometrically exact approach for dynamics of finite-strain rods undergoing large motions. Hodges (1990) developed a mixed variational formulation based on exact intrinsic equations for dynamics of moving beams. Robotic manipulators and mechanisms are examples of flexible multibody systems undergoing large displacements and rotations. Quadrelli and Atluri (1996, 1998) analysed flexible multibody systems with spatial beams using primal and mixed variational principles. Rochinha and Sampaio (2000) proposed an approach for numerical modelling of large overall motions of multibody systems. A consistent theory of finite stretches and finite rotations, in space-curved beams of arbitrary cross-section was given by Atluri, Iura & Vasudevan (2001). Okamoto & Omura (2003) performed a dynamic analysis for a flexible structure undergoing large translational and rotational displacements when moving along a nonlinear trajectory at variable velocity. Large displacement analysis of a space frame was carried out by Ijima, Obiwa, Iguchi and Goto (2003). A nonlinear formulation of the Meshless Local Petrov-Galerkin (MLPG) finite-volume mixed method was developed for the large deformation analysis of static and dynamic problems by Han, Rajendran and Atluri (2005). A dynamic analysis of a thin shell undergoing large displacements and rotations was carried out by Majorana and Salomoni (2008). Meshless Local Petrov-Galerkin (MLPG) approach can be applied to solve problems with large deformations and rotations (Han, Liu, Rajendran and Atluri 2006, Atluri, Liu and Han 2006a, 2006b). A geometrically nonlinear analysis of Reissner-Mindlin plate by meshless computation was performed by Wen and Hon (2007). A smoothed finite element method was presented by Cui et al. (2008) to analyze linear and geometrically nonlinear problems of plates and shells using bilinear quadrilateral elements. Geometrically nonlinear solid shell elements were used by Lee, Wu, Clarke and Lee (2008) for modeling of a lightweight composite space reflector. Wong and Shie (2008) proposed a Galerkin-based smoothed particle hydrodynamics (SPH) formulation for large deformation analysis.

Dynamics of a flexible beam undergoing finite rotations has been formulated by several approaches (Iura and Atluri 1995): an inertial approach, a floating approach, a co-rotational approach and a convected coordinate approach. When the inertial frame approach is used, a highly non-linear beam theory is necessary to simulate the motion of beams undergoing finite rotations (see e.g. Bathe, Ramm and Wilson 1975, Geradin and Cardona 1989, Iura and Atluri 1988a, 1988b, 1989, Simo and Vu-Quoc 1986). In floating frame approach (see e.g. Simo and Vu-Quoc

1986), strains of the system are measured relative to a floating frame assuming small strains of the body undergoing finite rigid displacements. A linear beam theory is employed to obtain the strain energy function, but the kinetic energy has a complicated expression and the equations of motion are highly coupled in the inertia terms. In co-rotational approach (see e.g. Argyris 1982, Hsiao and Jang 1991), a rotating frame is introduced to describe the elastic motion of the body and also to derive the kinetic energy function. A transformation of the displacement components between global and local coordinates is used to define the equations of motion in terms of a fixed global coordinate system. The co-rotational approach is different from the floating frame approach in the sense that the constraint equations do not appear explicitly in the co-rotational approach. Alternate stress and conjugate strain measures involving rigid rotations of finitely deformed plates and shells were given by Atluri (1984). A survey of variational principles, which form the basis for computational methods in both continuum mechanics and multi-rigid body dynamics and explicit use of the finite rotation tensor was presented by Atluri and Cazzani (1994). Iura and Atluri (2003) gave a review of advances made in the approaches used to describe finite rotations in structural mechanics. An accuracy of finite element solutions for 3-D Timoshenko's beams, obtained using a co-rotational formulation, was discussed by Iura, Suetake and Atluri (2003). Liu (2006) carried out computations of large rotation through an index two Nilpotent equation. Kulikov and Plotnikova (2008) developed a finite rotation geometrically exact four-node solid-shell element. Parameterisation of large rotations in co-rotational beam and shell elements was studied by Battini (2008). In convected coordinate approach, the inertial and external forces are evaluated in the fixed global coordinates, while the internal forces are calculated from the stress components measured in the convected coordinates (see e.g. Belytschko and Hsieh 1973). In the present work, both an inertial frame and a floating (moving) frame are employed to study the vehicle dynamics. The kinetic energy of the system is obtained with respect to an inertial frame in terms of displacements and rotation of the floating frame and elastic displacements relative to the floating frame. The strain energy of the system is obtained with respect to the floating frame, assuming small strains.

In the present work, a detailed linear analysis of the problem of dynamic instabilities in slender space launch vehicles is undertaken. This model includes important effects of flexible body dynamics, such as velocity induced curvature effects, which have not been considered so far in the published literature. The new aspect in the proposed analysis approach is the use of total derivatives of displacements in a Lagrangian framework. The present model incorporates the effect of aerodynamic forces and the thrust of the vehicle, accounting for variable mass of the system. The present model was used to investigate the onset of the aeroelastic instability of

a slender launch vehicle by Trikha, Mahapatra, Gopalakrishnan & Pandiyan (2008). Also, the effect of combustion coupled follower force and mass sensitivity on the stability of a launch vehicle was studied by Trikha, Gopalakrishnan, Mahapatra & Pandiyan (2008). The vehicle is idealised as a free-free beam with assembled segments and their respective effective stiffness and mass approximations. In section 2, a mathematical model of a space launch vehicle is developed. In section 3, forces acting on a space launch vehicle during its flight are discussed. Next, a *h-p* finite element model is developed for numerical simulations in section 4. In section 5, numerical simulations are carried out for a representative vehicle to determine the instability regimes with respect to vehicle speed (Mach number) and propulsive thrust as parameters. The phenomena of static instability (divergence) and dynamic instability (flutter) are observed for certain parameters. The results at low Mach number match closely with the results obtained from previous models published in the literature.

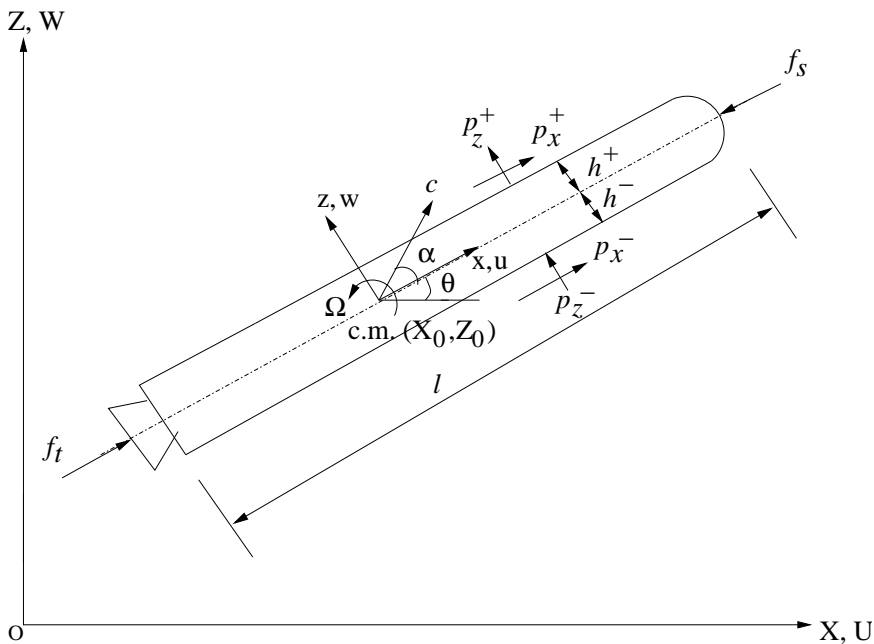


Figure 1: Schematic configuration of a vehicle and the coordinate system.

2 Mathematical Model

A one-dimensional approximation of a slender space launch vehicle is considered here. As shown in figure 1, the model of the vehicle is composed of a long cylindrical segment in the middle and a nose region in the front. The long cylindrical segment may consist of a single rocket motor (single stage vehicle) or multiple rocket motors (multi-stage vehicle). A vehicle stage may be a solid propellant rocket motor, a liquid propellant rocket motor or a hybrid rocket motor with a nozzle at the end. Let us first consider a vehicle having length l and cross sectional area A . When the launch vehicle has asymmetry about the vehicle axis, then the three-dimensional deformations and forces need to be considered. As an approximation, the vehicle motion is studied in a two-dimensional plane. The motion of the vehicle is studied in inertial axes X - Z . The motion of the vehicle is assumed to be in the XZ plane involving translation in longitudinal and transverse directions and pitching motion in the XZ plane. The coordinates of the center of mass (c.m.) of the vehicle in the inertial axes are given by $(X_0(t), Z_0(t))$. The elastic displacements of the vehicle are described in the body-fixed axes or the local axes x - z . The origin of the body-fixed axes is attached at (X_0, Z_0) (see figure 1). Vehicle axis is assumed to be along the body fixed x -axis. Let θ be the angle between the vehicle axis (x -axis of the body fixed frame) and X -axis of the inertial frame. The coordinates of a material point in the vehicle with respect to the body-fixed frame are given by (x, z) . The coordinates of the same material point in the inertial frame at time t are given by

$$\begin{aligned} X(t) &= X_0 + (x \cos \theta - z \sin \theta) = X_0 + x' , \\ Z(t) &= Z_0 + (x \sin \theta + z \cos \theta) = Z_0 + z' , \end{aligned} \quad (1)$$

where $x' = (x \cos \theta - z \sin \theta)$ and $z' = (x \sin \theta + z \cos \theta)$. Let U and W be the components of total displacement of a material point in the vehicle at time t with respect to the inertial frame of reference. Let $u(x, z, t)$ and $w(x, z, t)$ be the axial displacement and the transverse displacement, respectively, with respect to the body-fixed coordinate system. Taking components of $u(x, z, t)$ and $w(x, z, t)$ in the inertial frame, we can write

$$\begin{aligned} u' &= u \cos \theta - w \sin \theta , \\ w' &= u \sin \theta + w \cos \theta , \end{aligned} \quad (2)$$

where $u'(X, Z, t)$ and $w'(X, Z, t)$ are the displacement components in the inertial frame (X, Z) respectively. Total displacement with respect to the inertial frame is given by

$$U = U_0 + u' , \quad W = W_0 + w' , \quad (3)$$

where U_0 and W_0 are the displacements of the center of mass coordinates (X_0, Z_0) at time t with respect to the inertial frame of reference. The velocity of the center of mass coordinates in the inertial frame is denoted by c , where the components of c in the inertial frame are given by

$$\frac{DX_0}{Dt} = \frac{DU_0}{Dt} = c \cos(\alpha + \theta), \quad \frac{DZ_0}{Dt} = \frac{DW_0}{Dt} = c \sin(\alpha + \theta), \quad (4)$$

where α is the angle of attack. When the total derivatives of displacements are introduced, the velocity components in the inertial frame are given by

$$\frac{DU}{Dt} = \frac{DU_0}{Dt} + \frac{Du'}{Dt}, \quad \frac{DW}{Dt} = \frac{DW_0}{Dt} + \frac{Dw'}{Dt}, \quad (5)$$

where

$$\begin{aligned} \frac{Du'}{Dt}(X, Z, t) &= \frac{\partial u'}{\partial t} + \frac{\partial u'}{\partial X} \frac{dX}{dt} + \frac{\partial u'}{\partial Z} \frac{dZ}{dt}, \\ \frac{Dw'}{Dt}(X, Z, t) &= \frac{\partial w'}{\partial t} + \frac{\partial w'}{\partial X} \frac{dX}{dt} + \frac{\partial w'}{\partial Z} \frac{dZ}{dt}. \end{aligned} \quad (6)$$

Differentiating equation (1) with respect to time and denoting $c'_x = dX_0/dt$ and $c'_z = dZ_0/dt$, we obtain

$$\begin{aligned} \frac{dX}{dt} &= \frac{dX_0}{dt} - \Omega(x \sin \theta + z \cos \theta) = c'_x - \Omega z', \\ \frac{dZ}{dt} &= \frac{dZ_0}{dt} + \Omega(x \cos \theta - z \sin \theta) = c'_z + \Omega x', \end{aligned} \quad (7)$$

where $\Omega = d\theta/dt$ denotes the angular velocity of the vehicle about the center of mass. We can write

$$\begin{aligned} \frac{\partial u'}{\partial X} &= \frac{\partial u'}{\partial x} \frac{\partial x}{\partial X} = \frac{\partial u'}{\partial x} \cos \theta, \quad \frac{\partial u'}{\partial Z} = \frac{\partial u'}{\partial z} \frac{\partial z}{\partial Z} = \frac{\partial u'}{\partial z} \cos \theta, \\ \frac{\partial w'}{\partial X} &= \frac{\partial w'}{\partial x} \cos \theta, \quad \frac{\partial w'}{\partial Z} = \frac{\partial w'}{\partial z} \cos \theta. \end{aligned} \quad (8)$$

Equation (6) is re-written using the terms obtained in equations (7) and (8), as

$$\begin{aligned} \frac{Du'}{Dt} &= \frac{\partial u'}{\partial t} + \frac{\partial u'}{\partial x} \cos \theta (c'_x - \Omega z') + \frac{\partial u'}{\partial z} \cos \theta (c'_z + \Omega x'), \\ \frac{Dw'}{Dt} &= \frac{\partial w'}{\partial t} + \frac{\partial w'}{\partial x} \cos \theta (c'_x - \Omega z') + \frac{\partial w'}{\partial z} \cos \theta (c'_z + \Omega x'). \end{aligned} \quad (9)$$

Note that in the works by several authors (e.g., Meirovitch & Wesley 1967; Murphy & Mermagen 2003; Beal 1965; Wu 1975, 1976), the terms $[(\partial u'/\partial X)(dX/dt) + (\partial u'/\partial Z)(dZ/dt)]$ and $[(\partial w'/\partial X)(dX/dt) + (\partial w'/\partial Z)(dZ/dt)]$ are neglected. Neglecting the effects due to these terms, which we call as ‘velocity induced curvature effects’, leads to the equations for a stationary beam. It results in decoupling of the rigid body modes and the flexible modes because of mode orthogonality for a stationary beam.

Our first objective is to construct the governing equations of motion for a general flexible lifting body segment by including the idealised effects of the aerodynamics, thrust and gravitational force. The vehicle segment is idealised as a slender beam with equivalent mass per unit length and equivalent cross-sectional area. The kinetic energy of the vehicle can be expressed as

$$\mathcal{T} = \frac{1}{2} \int_l \int_A \rho \left[\left\{ \frac{DU}{Dt} \right\}^2 + \left\{ \frac{DW}{Dt} \right\}^2 \right] dAdx$$

Using equations (4), (5) and (9) and after simplification we obtain

$$\begin{aligned} \mathcal{T} = & \frac{1}{2} \int_l \int_A \rho \left[c^2 + \dot{u}^2 + \dot{w}^2 + 2c_x \dot{u} + 2c_z \dot{w} + \Omega^2 (u^2 + w^2) + 2\Omega (uc_z - wc_x) \right. \\ & + 2\Omega (u\dot{w} - w\dot{u}) + (c'_x - \Omega z')^2 \cos^2 \theta \left\{ \left(\frac{\partial u}{\partial x} \right)^2 + \left(\frac{\partial w}{\partial x} \right)^2 \right\} \\ & + (c'_z + \Omega x')^2 \cos^2 \theta \left\{ \left(\frac{\partial u}{\partial z} \right)^2 + \left(\frac{\partial w}{\partial z} \right)^2 \right\} \\ & + 2(c'_x - \Omega z') \cos \theta \left\{ c_x \frac{\partial u}{\partial x} + c_z \frac{\partial w}{\partial x} + \dot{u} \frac{\partial u}{\partial x} + \dot{w} \frac{\partial w}{\partial x} + \Omega \left(u \frac{\partial w}{\partial x} - w \frac{\partial u}{\partial x} \right) \right\} \\ & + 2(c'_z + \Omega x') \cos \theta \left\{ c_x \frac{\partial u}{\partial z} + c_z \frac{\partial w}{\partial z} + \dot{u} \frac{\partial u}{\partial z} + \dot{w} \frac{\partial w}{\partial z} + \Omega \left(u \frac{\partial w}{\partial z} - w \frac{\partial u}{\partial z} \right) \right\} \\ & \left. + 2(c'_x - \Omega z')(c'_z + \Omega x') \cos^2 \theta \left\{ \frac{\partial u}{\partial x} \frac{\partial u}{\partial z} + \frac{\partial w}{\partial x} \frac{\partial w}{\partial z} \right\} \right] dAdx, \end{aligned} \quad (10)$$

where $c_x = c \cos \alpha$ is the component of velocity of the center of mass coordinates along the vehicle axis and $c_z = c \sin \alpha$ is the component of velocity perpendicular to the vehicle axis (see figure 1). Considering the elementary beam theory (Euler-Bernoulli beam theory), the axial displacement field within the vehicle segment can be expressed as

$$u(x, z, t) = u^\circ(x, t) - z \frac{\partial}{\partial x} w(x, t), \quad (11)$$

where $u(x, z, t)$ is the longitudinal displacement of a point on the vehicle cross-section, $u^\circ(x, t)$ is the longitudinal displacement along the vehicle axis and $w(x, t)$ is the transverse displacement of the vehicle cross-section. The positive z -coordinate of the upper half surface of the vehicle segment is denoted by h^+ and the negative z -coordinate of the lower half surface of the vehicle segment is denoted by h^- . The axial strain is given by

$$\epsilon_{xx} = \frac{\partial u}{\partial x}. \quad (12)$$

The strain energy stored due to mechanical deformation, can be expressed as

$$\mathcal{U} = \frac{1}{2} \int_l \int_A \sigma_{xx} \epsilon_{xx} dA dx, \quad (13)$$

where $\sigma_{xx} = E \epsilon_{xx}$ and E is the equivalent elastic modulus of the vehicle segment cross-section.

Work done on the system can be divided into two parts: one is the work done by the conservative forces and the other is the work done by the non-conservative forces. Work done by the conservative axial force $P(x)$ is given by

$$\mathcal{W}_c = \frac{1}{2} \int_l P(x) \left(\frac{\partial w}{\partial x} \right)^2 dx. \quad (14)$$

The work done on the system by the aerodynamic forces can be expressed as

$$\mathcal{W}_a = \int_l \left[p_x^+ (u^\circ - h^+ \frac{\partial w}{\partial x}) + p_x^- (u^\circ - h^- \frac{\partial w}{\partial x}) + (p_z^+ + p_z^-) w \right] dx, \quad (15)$$

where p_x^\pm are the resultant aerodynamic shear forces per unit length on the centerline of the upper half and the lower half surfaces of a vehicle segment and p_z^\pm are the resultant aerodynamic pressure per unit length on the centerline of the upper half and the lower half surfaces. The aerodynamic forces are non-conservative in nature. Distribution of the aerodynamic forces along the length of the vehicle can be determined from wind/shock tunnel tests or actual flight data.

The work done on the system due to the non-conservative follower forces can be expressed as

$$\mathcal{W}_f = f_s u_s - f_s w_s \left[\frac{\partial w}{\partial x} \right]_{x=x_s} + f_t u_t - f_t w_t \left[\frac{\partial w}{\partial x} \right]_{x=x_t}, \quad (16)$$

where f_t is the thrust acting on the vehicle, f_s is the drag force acting on the nose of the vehicle, f_t and f_s are the follower forces. Presence of both types of forces f_t and

f_s represent a general case. Depending on the special boundaries; that is the nose region or the nozzle, f_t and f_s are to be approximated. For intermediate segments, either $f_s = 0$, $f_t = 0$, or these may have other form of physical representation (e.g., active control surfaces, auxiliary thruster etc.).

Work done by the gravitational force can be expressed as

$$\mathcal{W}_g = \int_l \int_A \rho (-a_g \cos \theta_g u - a_g \sin \theta_g w) dA dx, \quad (17)$$

where a_g is the acceleration due to the gravitational force and θ_g is the angle of the gravitational force vector relative to the vehicle axis. By using the Extended Hamilton's principle, one has

$$\delta \int_{t_1}^{t_2} \mathcal{L} dt + \int_{t_1}^{t_2} \delta \mathcal{W}_{nc} dt = 0, \quad (18)$$

where the Lagrangian $\mathcal{L} = \mathcal{T} - \mathcal{U} + \mathcal{W}_c + \mathcal{W}_g$ and $\mathcal{W}_{nc} = \mathcal{W}_f + \mathcal{W}_a$, we arrive at the following two governing equations in (u°, w) ; that is,

$$\begin{aligned} & -\rho A \dot{c}_x - \rho A \ddot{u}^\circ + \rho I_1 \ddot{w}_{,x} - \rho \cos^2 \theta \{a^2 A + b^2 I_2 - 2ab I_1\} u^{\circ,xx} \\ & - 2\rho \cos \theta \{aA - bI_1\} \ddot{u}^{\circ, x} - \rho \{(\dot{a}A - \dot{b}I_1) \cos \theta - (aA - bI_1) \Omega \sin \theta\} u^{\circ, x} \\ & + \rho \cos \theta \{gA - hI_1\} \dot{w}_{,x} + \rho \{(\dot{g}A - \dot{h}I_1) \cos \theta - (gA - hI_1) \Omega \sin \theta\} w_{,x} \\ & + \rho \{(agA - (bg + ah)I_1 + bhI_2) \cos^2 \theta\} w_{,xx} \\ & + \rho \Omega \cos^2 \theta \{(aA - bI_1) \cos \theta - (gA - hI_1) \sin \theta\} w_{,x} \\ & + \rho \cos^2 \theta \{a^2 I_1 + b^2 I_3 - 2ab I_2\} w_{,xxx} \\ & + 2\rho \cos \theta \{aI_1 - bI_2\} \dot{w}_{,xx} + 2\rho \Omega \cos \theta \{aA - bI_1\} w_{,x} \\ & + \rho \cos \theta \{(\dot{a}I_1 - \dot{b}I_2) \cos \theta - (aI_1 - bI_2) \Omega \sin \theta\} w_{,xx} + \rho \Omega^2 (Au^\circ - I_1 w_{,x}) + \rho \Omega c_z A \\ & + \rho \Omega A \dot{w} + A \frac{d}{dt} (\rho \Omega w) + EA u^{\circ, xx} - EI_1 w_{,xxx} \\ & = \rho A a_g \cos \theta_g - [p_x^+ + p_x^-] - P(x), \end{aligned} \quad (19)$$

for axial motion, and

$$\begin{aligned}
& -\rho A(\dot{c}_z + \Omega c_x) + \rho A \Omega c_x \cos^2 \theta + \rho I_2 \ddot{w}_{,xx} - \rho I_1 \ddot{u}^{\circ}_{,x} \\
& + \rho \cos^2 \theta \{a^2 I_2 + b^2 I_4 - 2ab I_3\} w_{,xxx} \\
& + \rho \{(\dot{a} I_2 - \dot{b} I_3) \cos \theta - (a I_2 - b I_3) \Omega \sin \theta\} w_{,xxx} \\
& - \rho A \ddot{w} - \rho [2\{(gA - hI_1) \Omega \cos^2 \theta\} w_{,x} + \{(g^2 A + h^2 I_2 - 2ghI_1) \cos^2 \theta\} w_{,xx}] \\
& + \rho [\{(gA - hI_1) \cos \theta\} \dot{u}^{\circ}_{,x} + \{\Omega \cos^2 \theta\} \dot{u}^{\circ}] - \rho \cos^2 \theta \{a^2 A + b^2 I_2 - 2ab I_1\} w_{,xxx} \\
& + 2\rho \cos \theta \{a I_2 - b I_3\} \dot{w}_{,xxx} + \rho \{(agA - (bg + ah)I_1 + bhI_2) \cos^2 \theta\} u^{\circ}_{,xx} \\
& + \rho \Omega \cos^2 \theta \{(aA - bI_1) \cos \theta - (gA - hI_1) \sin \theta\} u^{\circ}_{,x} \\
& + \rho \Omega \cos^2 \theta \{(aI_1 - bI_2) \cos \theta - (gI_1 - hI_2) \sin \theta\} w_{,xx} - 2\rho \cos \theta \{aA - bI_1\} \dot{w}_{,x} \\
& - EI_2 w_{,xxxx} - \rho \{(\dot{a}A - \dot{b}I_1) \cos \theta - (aA - bI_1) \Omega \sin \theta\} w_{,x} \\
& - \rho \cos^2 \theta \{a^2 I_1 + b^2 I_3 - 2ab I_2\} u^{\circ}_{,xxx} - 2\rho \cos \theta \{aI_1 - bI_2\} \dot{u}^{\circ}_{,xx} \\
& + \rho \frac{d}{dt} [\{(gI_1 - hI_2) \cos \theta\} w_{,xx} + I_1 \{\Omega \cos^2 \theta\} w_{,x}] - \rho \Omega^2 I_1 \{\sin 2\theta \cos^2 \theta\} w_{,x} \\
& - (P(x) w_{,x})_{,x} + EI_1 u^{\circ}_{,xxx} \\
& + \rho \Omega^2 I_1 u^{\circ}_{,x} - \rho \Omega^2 I_2 w_{,xx} - 2\rho \Omega A \dot{u}^{\circ} - 2\rho \Omega \cos \theta \{aA - bI_1\} u^{\circ}_{,x} + 3\rho \Omega I_1 \dot{w}_{,x} \\
& + 4\rho \Omega \cos \theta \{aI_1 - bI_2\} w_{,xx} + I_1 \frac{d}{dt} (\rho \Omega w_{,x}) + h^+ (p_x^+)_{,x} + h^- (p_x^-)_{,x} \\
& = \rho A a_g \sin \theta_g - [p_z^+ + p_z^-],
\end{aligned} \tag{20}$$

for transverse motion. Here $a = (c'_x - \Omega x \sin \theta)$, $b = \Omega \cos \theta$, $g = (c'_z + \Omega x \cos \theta)$, $h = \Omega \sin \theta$ and $[I_1, I_2, I_3, I_4] = \int_A [z, z^2, z^3, z^4] dA$ represents the effective area moments of the vehicle segment. $(\cdot)_{,x}$ denotes partial derivative of displacements with respect to x .

Boundary conditions for the vehicle segment are given by

$$\begin{aligned}
& \rho \cos^2 \theta \{a^2 A + b^2 I_2 - 2ab I_1\} u^{\circ}_{,x} - EA u^{\circ}_{,x} + \rho \cos \theta \{aA - bI_1\} \dot{u}^{\circ} \\
& - \rho \{(agA - (bg + ah)I_1 + bhI_2) \cos^2 \theta\} w_{,x} + EI_1 w_{,xx} \\
& - \rho \cos^2 \theta \{a^2 I_1 + b^2 I_3 - 2ab I_2\} w_{,xx} - \rho \cos \theta \{aI_1 - bI_2\} \dot{w}_{,x} + \rho c_x \cos \theta \{aA - bI_1\} \\
& - \rho \Omega \cos \theta \{aA - bI_1\} w + f_s + f_t \\
& = 0
\end{aligned} \tag{21}$$

for axial force balance,

$$\begin{aligned}
& -\rho I_2 \ddot{w}_{,x} + \rho I_1 \ddot{u}^\circ + EI_2 w_{,xxx} - \rho \cos^2 \theta \{a^2 I_2 + b^2 I_4 - 2ab I_3\} w_{,xxx} \\
& + \rho \{(g^2 A + h^2 I_2 - 2gh I_1) \cos^2 \theta\} w_{,x} - 2\rho \cos \theta \{a I_2 - b I_3\} \dot{w}_{,xx} \\
& - \rho \{(gA - h I_1) \cos \theta\} \dot{u}^\circ - \rho \{(\dot{a} I_2 - \dot{b} I_3) \cos \theta - (a I_2 - b I_3) \Omega \sin \theta\} w_{,xx} \\
& - \rho \{(agA - (bg + ah) I_1 + bh I_2) \cos^2 \theta\} u^\circ_{,x} + \rho \cos^2 \theta \{a^2 A + b^2 I_2 - 2ab I_1\} w_{,x} \\
& + \rho \cos \theta \{aA - b I_1\} \dot{w} + \rho \cos^2 \theta \{a^2 I_1 + b^2 I_3 - 2ab I_2\} u^\circ_{,xx} - EI_1 u^\circ_{,xx} \\
& - \rho \Omega \cos^2 \theta \{(a I_1 - b I_2) \cos \theta - (g I_1 - h I_2) \sin \theta\} w_{,x} \\
& + 2\rho \cos \theta \{a I_1 - b I_2\} \dot{u}^\circ_{,x} - \rho \frac{d}{dt} \{(g I_1 - h I_2) \cos \theta\} w_{,x} - 3\rho \Omega \cos \theta \{a I_1 - b I_2\} w_{,x} \\
& - \rho c_x \{(gA - h I_1) \cos \theta\} + \rho c_z \cos \theta \{aA - b I_1\} - \rho \Omega^2 I_1 u^\circ + \rho \Omega^2 I_2 w_{,x} - \rho \Omega c_z I_1 \\
& + \rho \Omega \cos \theta \{aA - b I_1\} u^\circ - \rho \Omega I_1 \dot{w} - I_1 \frac{d}{dt} (\rho \Omega w) + \rho \Omega \{(gA - h I_1) \cos \theta\} w \\
& = h^+ p_x^+ + h^- p_x^- + f_s[w_{,x}]_s + f_t[w_{,x}]_t
\end{aligned} \tag{22}$$

for transverse force balance, and

$$\begin{aligned}
& [\rho \cos^2 \theta \{a^2 I_2 + b^2 I_4 - 2ab I_3\} - EI_2] w_{,xx} + \rho \cos \theta \{a I_2 - b I_3\} \dot{w}_{,x} \\
& + [EI_1 - \rho \cos^2 \theta \{a^2 I_1 + b^2 I_3 - 2ab I_2\}] u^\circ_{,x} - \rho \cos \theta \{a I_1 - b I_2\} \dot{u}^\circ \\
& - \rho c_x \cos \theta \{a I_1 - b I_2\} + \rho \{(ag I_1 - (bg + ah) I_2 + bh I_3) \cos^2 \theta\} w_{,x} \\
& + \rho \Omega \cos \theta \{a I_1 - b I_2\} w \\
& = f_s w_s + f_t w_t
\end{aligned} \tag{23}$$

for angular moment balance.

Considering a special case of $\theta = 0$, we obtain $a = c_x$, $b = \Omega$, $g = (c_z + \Omega x)$, $h = 0$ and substituting in the governing equations (19)-(20) we obtain

$$\begin{aligned}
& -\rho A \dot{c}_x - \rho A \ddot{u}^\circ + \rho I_1 \ddot{w}_{,x} - \rho \{c_x^2 A + \Omega^2 I_2 - 2c_x \Omega I_1\} u^\circ_{,xx} \\
& - 2\rho \{c_x A - \Omega I_1\} \dot{u}^\circ_{,x} - \rho (\dot{c}_x A - \dot{\Omega} I_1) u^\circ_{,x} \\
& + \rho A (c_z + \Omega x) \dot{w}_{,x} + \rho A (\dot{c}_x + \dot{\Omega} x) w_{,x} \\
& + \rho (c_z + \Omega x) \{c_x A - \Omega I_1\} w_{,xx} + \rho \Omega \{c_x A - \Omega I_1\} w_{,x} + \rho \Omega^2 (A u^\circ - I_1 w_{,x}) \\
& + \rho \{c_x^2 I_1 + \Omega^2 I_3 - 2c_x \Omega I_2\} w_{,xxx} + 2\rho \{c_x I_1 - \Omega I_2\} \dot{w}_{,xx} \\
& + 2\rho \Omega \{c_x A - \Omega I_1\} w_{,x} + \rho \{\dot{c}_x I_1 - \dot{\Omega} I_2\} w_{,xx} \\
& + \rho \Omega c_z A + \rho \Omega A \dot{w} + A \frac{d}{dt} (\rho \Omega w) + E A u^\circ_{,xx} - EI_1 w_{,xxx} \\
& = \rho A a_g \cos \theta_g - [p_x^+ + p_x^-] - P(x),
\end{aligned} \tag{24}$$

for axial motion, and

$$\begin{aligned}
& -\rho A \dot{c}_z + \rho I_2 \ddot{w}_{,xx} - \rho I_1 \ddot{u}^{\circ}_{,x} + \rho \{c_x^2 I_2 + \Omega^2 I_4 - 2c_x \Omega I_3\} w_{,xxxx} + \rho \{\dot{c}_x I_2 - \dot{\Omega} I_3\} w_{,xxx} \\
& - \rho A \ddot{w} - \rho [2(c_z + \Omega x) A \Omega w_{,x} + (c_z + \Omega x)^2 A w_{,xx}] + \rho [(c_z + \Omega x) A \dot{u}^{\circ}_{,x} + \Omega \dot{u}^{\circ}] \\
& - \rho \{c_x^2 A + \Omega^2 I_2 - 2c_x \Omega I_1\} w_{,xx} + 2\rho \{c_x I_2 - \Omega I_3\} \dot{w}_{,xxx} \\
& + \rho \{c_x A (c_z + \Omega x) - \Omega I_1 (c_z + \Omega x)\} u^{\circ}_{,xx} + \rho \Omega \{c_x A - \Omega I_1\} u^{\circ}_{,x} \\
& + \rho \Omega \{c_x I_1 - \Omega I_2\} w_{,xx} - 2\rho \{c_x A - \Omega I_1\} \dot{w}_{,x} - \rho \{\dot{c}_x A - \dot{\Omega} I_1\} w_{,x} \\
& - \rho \{c_x^2 I_1 + \Omega^2 I_3 - 2c_x \Omega I_2\} u^{\circ}_{,xxx} - 2\rho \{c_x I_1 - \Omega I_2\} \dot{u}^{\circ}_{,xx} - E I_2 w_{,xxxx} \\
& + \rho \frac{d}{dt} [(c_z + \Omega x) I_1 w_{,xx} + I_1 \Omega w_{,x}] - (P(x) w_{,x})_{,x} + E I_1 u^{\circ}_{,xxx} \\
& + \rho \Omega^2 I_1 u^{\circ}_{,x} - \rho \Omega^2 I_2 w_{,xx} - 2\rho \Omega A \dot{u}^{\circ} - 2\rho \Omega \{c_x A - \Omega I_1\} u^{\circ}_{,x} + 3\rho \Omega I_1 \dot{w}_{,x} \\
& + 4\rho \Omega \{c_x I_1 - \Omega I_2\} w_{,xx} + I_1 \frac{d}{dt} (\rho \Omega w_{,x}) + h^+(p_x^+)_{,x} + h^-(p_x^-)_{,x} \\
& = \rho A a_g \sin \theta_g - [p_z^+ + p_z^-],
\end{aligned} \tag{25}$$

for transverse motion.

Further in this paper, we consider the special case of $\theta = 0$. There are inherent inhomogeneities involved if angular velocity (Ω) is considered, that is, when the terms involving Ωx is considered. For numerical simplicity, we neglect the terms involving Ω . The effect of inhomogeneous terms due to Ωx will be considered in a future work. The governing equations contain several time varying coefficients. For simplicity, in this paper, only a quasi-linearised form of the governing equations is considered; that is, the analysis is carried out for assumed state of translational velocities. Neglecting the terms involving Ω in the equations (24)-(25), we obtain

$$\begin{aligned}
& -\rho A \dot{c}_x - \rho A \ddot{u}^{\circ} + \rho I_1 \ddot{w}_{,x} - \rho A c_x^2 u^{\circ}_{,xx} - 2\rho A c_x \dot{u}^{\circ}_{,x} - \rho A \dot{c}_x u^{\circ}_{,x} + \rho A c_z \dot{w}_{,x} + \rho A \dot{c}_z w_{,x} \\
& + \rho A c_x c_z w_{,xx} + \rho I_1 c_x^2 w_{,xxx} + 2\rho I_1 c_x \dot{w}_{,xx} + \rho I_1 \dot{c}_x w_{,xx} + E A u^{\circ}_{,xx} - E I_1 w_{,xxx} \\
& = \rho A a_g \cos \theta_g - [p_x^+ + p_x^-] - P(x),
\end{aligned} \tag{26}$$

for axial motion, and

$$\begin{aligned}
& -\rho A \dot{c}_z + \rho I_2 \ddot{w}_{,xx} - \rho I_1 \ddot{u}^{\circ}_{,x} + \rho I_2 c_x^2 w_{,xxxx} + \rho I_2 \dot{c}_x w_{,xxx} - \rho A \ddot{w} - \rho A c_z^2 w_{,xx} \\
& + \rho A c_z \dot{u}^{\circ}_{,x} + 2\rho I_2 c_x \dot{w}_{,xxx} + \rho A c_x c_z u^{\circ}_{,xx} - 2\rho A c_x \dot{w}_{,xx} - \rho A \dot{c}_x w_{,xx} \\
& - \rho I_1 c_x^2 u^{\circ}_{,xxx} - \rho A c_x^2 w_{,xx} - 2\rho I_1 c_x \dot{u}^{\circ}_{,xx} + \rho I_1 \dot{c}_x w_{,xx} - E I_2 w_{,xxxx} - (P(x) w_{,x})_{,x} \\
& + E I_1 u^{\circ}_{,xxx} + h^+(p_x^+)_{,x} + h^-(p_x^-)_{,x} \\
& = \rho A a_g \sin \theta_g - [p_z^+ + p_z^-],
\end{aligned} \tag{27}$$

for transverse motion. Corresponding rigid body equation of motion along the vehicle axis direction is given by

$$-\rho A \dot{c}_x = \rho A a_g \cos \theta_g - [p_x^+ + p_x^-] - P(x). \quad (28)$$

Corresponding rigid body equation of motion perpendicular to the vehicle axis direction is given by

$$-\rho A \dot{c}_z = \rho A a_g \sin \theta_g - [p_z^+ + p_z^-]. \quad (29)$$

By comparing equations (26)-(28) and (27)-(29), we obtain the condition under which a flexible body with internal stress waves behaves like a perfect rigid body. This condition is given by the following equations:

$$\begin{aligned} & -\rho A \ddot{u}^\circ + \rho I_1 \ddot{w}_{,x} - \rho A c_x^2 u^\circ_{,xx} - 2\rho A c_x \dot{u}^\circ_{,x} - \rho A \dot{c}_x u^\circ_{,x} + \rho A c_z \dot{w}_{,x} + \rho A \dot{c}_z w_{,x} \\ & + \rho A c_x c_z w_{,xx} + \rho I_1 c_x^2 w_{,xxx} + 2\rho I_1 c_x \dot{w}_{,xx} + \rho I_1 \dot{c}_x w_{,xx} + E A u^\circ_{,xx} - E I_1 w_{,xxx} \\ & = 0, \end{aligned} \quad (30)$$

for axial vibrations, and

$$\begin{aligned} & \rho I_2 \ddot{w}_{,xx} - \rho I_1 \ddot{u}^\circ_{,x} + \rho I_2 c_x^2 w_{,xxx} + \rho I_2 \dot{c}_x w_{,xxx} - \rho A \ddot{w} - \rho A c_z^2 w_{,xx} \\ & - \rho A c_x^2 w_{,xx} + \rho A c_z \dot{u}^\circ_{,x} + 2\rho I_2 c_x \dot{w}_{,xxx} + \rho A c_x c_z u^\circ_{,xx} - 2\rho A c_x \dot{w}_{,x} \\ & - \rho A \dot{c}_x w_{,x} - \rho I_1 c_x^2 u^\circ_{,xxx} - 2\rho I_1 c_x \dot{u}^\circ_{,xx} \\ & + \rho I_1 \dot{c}_z w_{,xx} - E I_2 w_{,xxx} - (P(x) w_{,x})_{,x} + E I_1 u^\circ_{,xxx} + h^+(p_x^+)_{,x} + h^-(p_x^-)_{,x} \\ & = 0, \end{aligned} \quad (31)$$

for transverse vibrations. In the next section, we consider the detailed nature of the forces acting on a launch vehicle.

3 Forces on a Launch Vehicle

A launch vehicle is subjected to aerodynamic forces, acoustic loads, thrust, forces due to combustion process, staging loads and the inertia forces during its flight. Here, we discuss the aerodynamic forces, the propulsive thrust, the axial forces and their approximation within the proposed modelling approach.

3.1 Aerodynamic Forces

A launch vehicle's motion in the atmosphere leads to aerodynamic forces and moments on the vehicle. A launch vehicle is designed to withstand these aerodynamic loads. The aerodynamic forces are also important factor for accurate prediction of

the vehicle's trajectory and performance. The aerodynamic forces are function of dynamic pressure q , angle of attack α and vehicle geometry. The dynamic pressure depends on the velocity of the vehicle c and the local atmospheric density ρ_a and it is given by $q = \frac{1}{2}\rho_a c^2$. The local atmospheric density is a function of altitude. The aerodynamic force is resolved into lift L and drag D . They are normal and parallel to the velocity vector, respectively, as shown in figure 2. It can also be resolved into a normal force N and a tangential force T , normal and parallel to the vehicle's reference axis. The resultant aerodynamic forces act at the centre of pressure (c.p.) of the vehicle. Classically, the aerodynamic forces are expressed in terms of dimensionless coefficients, so that lift and drag are expressed as $L = C_L q S$, $D = C_D q S$, where C_L and C_D are lift and drag coefficients respectively and S is the reference cross section area. The aerodynamic coefficients can also be written for the forces resolved in the vehicle axis system. The normal force coefficient is denoted as C_N and the axial force coefficient as C_A .

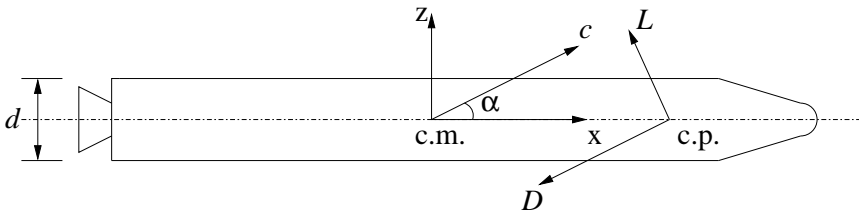


Figure 2: Schematic diagram showing drag force D and lift force L on a vehicle. c is the velocity of the vehicle.

The aerodynamic coefficients are function of Mach number (M_∞), angle of attack and Reynolds number. The Mach number is defined as $M_\infty = c/c_o$, where c_o is the speed of sound at standard atmospheric conditions. The aerodynamic coefficients can be obtained either experimentally or by Computational Fluid Dynamics (CFD) analysis. The aerodynamic coefficients are determined experimentally from wind tunnel tests or flight tests. A procedure for computing the aerodynamic coefficients for different vehicle configurations for a wide range of angles of attack and Mach numbers is given by Jorgensen (1973). The procedure is valid for subsonic to supersonic Mach numbers. In this procedure, the normal force coefficient derived by Allen and Perkins (1951) based on the slender body theory and the cross flow theory are given by

$$C_N = \frac{1}{S} \sin 2\alpha \cos \frac{\alpha}{2} \int_0^l \frac{dS}{dx} dx + \eta C_{dn} \frac{\sin^2 \alpha}{S} \int_0^l d(x) dx . \quad (32)$$

For small angles of attack, C_N can be written as

$$C_N = \frac{2\alpha}{S} \int_0^l \frac{dS}{dx} dx + \eta C_{dn} \frac{\alpha^2}{S} \int_0^l d(x) dx . \quad (33)$$

Here C_{dn} is the crossflow drag coefficient, η is the crossflow drag proportionality factor (Jorgensen 1973) and $d(x)$ is the diameter of the cross-section at distance x . The first term in this expression is due to the slender body theory and second term is contributed by the cross flow theory. According to the slender body theory, a normal force is produced at the conical nose region for non-zero angle of attack. On the cylindrical segments of the vehicle, the normal force is negligible since it is not a lifting body. The cross flow theory includes the normal force due to fluid viscosity.

In order to investigate the stability characteristics of the launch vehicles, it is important to know the variation in the aerodynamic forces with small changes in the system parameters. As shown by Cornelisse, Schoyer and Wakker (1979), the aerodynamic forces can be expanded in a Taylor series, and by neglecting higher order terms, one can write

$$F = F_0 + \frac{\partial F}{\partial \alpha} \alpha + \frac{\partial F}{\partial \dot{\alpha}} \dot{\alpha} + \frac{\partial F}{\partial \Omega} \Omega , \quad (34)$$

where F_0 is a constant and it is zero for a symmetric vehicle, $\dot{\alpha}$ is the rate of change of angle of attack. The normal force is calculated based on the effective angle of attack $\alpha(x, t)$ as given by Platus (1992). The effective angle of attack is expressed as

$$\alpha(x, t) = \alpha - w_{,x} + \frac{1}{c_x} \dot{w} . \quad (35)$$

The last two terms in equation (34) due to the angular velocity of the vehicle and the rate of change of angle of attack, represent unsteady aerodynamics. The effects due to unsteady aerodynamics have been neglected in the present paper for simplicity, as this would involve coupled unsteady flow computations. This aspect will be considered in a future work. By neglecting the last two terms in equation (34), the aerodynamic pressure per unit length is expressed as

$$p_z(x, t) = \frac{\partial p_z}{\partial \alpha}(x) \alpha(x, t) , \quad (36)$$

where $p_z = C_N q S$. Substituting the form of $\alpha(x, t)$ from equation (35) in equation (36), one gets

$$p_z(x, t) = \frac{\partial p_z}{\partial \alpha}(x) \left[\alpha - w_{,x} + \frac{1}{c_x} \dot{w} \right] . \quad (37)$$

The aerodynamic drag can be split into the following main components: wave drag from the nose region due to the presence of shock waves which occurs at supersonic and hypersonic speeds. Second one is the viscous drag due to the skin friction which is the main drag component at subsonic speeds. The other main component is the base drag due to the wake behind the vehicle and it is strongly affected by the shape of the vehicle. The axial force per unit length is given as $p_x = C_A q S$. The axial force coefficients for a nose-cone configuration can be determined empirically as given by Jorgensen (1973) and Cornelisse, Schoyer and Wakker (1979). The drag force at the nose region is given by $f_s = C_A q S$, where C_A is the axial force coefficient at the nose region given by

$$C_A = \left(0.083 + \frac{0.096}{M_\infty^2} \right) (5.73 * \theta)^{1.69}, \quad M_\infty > 1 \quad (38)$$

and θ is the half cone angle in radians. The axial force per unit length due to the viscous drag is given by $p_x = C_{AB} q S / l$, where S is the wetted (circumferential) surface area of the vehicle and C_{AB} is the axial force coefficient due to the viscous drag given by

$$C_{AB} = C_{Df} \cos^2 \alpha, \quad C_{Df} = \frac{0.427}{(\log_{10} R_e - 0.407)^{2.64}}, \quad R_e = \frac{\rho_a c l}{\mu}, \quad (39)$$

where C_{Df} is the viscous drag coefficient for turbulent flow, R_e is the Reynolds number and μ is the dynamic viscosity of air. For most of the large launch vehicles, the boundary layer may be assumed as turbulent. The transition from laminar to turbulent flow takes place around $R_e = 10^6$ based on the vehicle length. Next, we consider the propulsive thrust and the combustion process in a rocket motor.

3.2 Propulsive thrust, combustion process and mass variation

All rocket motors of a launch vehicle are based on the combustion of propellants in a combustion chamber, production of hot combustion gases and expansion of these hot gases through a nozzle. The expulsion of combustion gases at high speed from the nozzle results in the reaction force (thrust) according to Newton's third law. The equations of motion of a rigid rocket were first given by Tsiolkovsky. The equation of motion in free space is given by (Cornelisse, Schoyer and Wakker 1979)

$$M(t) \frac{dc}{dt} = \dot{m} V_e, \quad V_e = \frac{2\gamma}{\gamma-1} R T_c \left[1 - \left(\frac{p_e}{p_c} \right)^{(\gamma-1)/\gamma} \right], \quad (40)$$

where $M(t)$ is the mass of the rocket at time t and is given as $M(t) = M_0 - \int_0^t \dot{m} dt$, M_0 is the initial vehicle mass at lift off and \dot{m} is the mass flow rate (due to combustion). For a constant thrust, the propellant consumption rate (\dot{m}) is constant and

$M(t) = M_0 - \dot{m}t$. The velocity of the rocket with respect to the inertial frame of reference is given as c . The exhaust velocity of the combustion gases with respect to the vehicle nozzle is given as V_e . T_c and p_c are the chamber temperature and pressure, respectively, p_e is the exhaust pressure at the nozzle exit, $\gamma = c_p/c_v$ defines the ratio of the specific heats, $R = R_0/\mathcal{M}$ defines the gas constant, R_0 is the universal gas constant and \mathcal{M} is the molecular weight of the gas. The combustion chamber conditions are assumed to be uniform throughout and the combustion gases are assumed to behave as ideal gases. The mass flow rate is obtained as

$$\dot{m} = \rho_e A_e V_e, \quad \rho_e = \rho_c \left(\frac{p_e}{p_c} \right)^{1/\gamma}, \quad (41)$$

where ρ_e is the gas density at the nozzle exit and A_e is the cross-sectional area at the nozzle exit. The thrust generated by the vehicle is given as

$$f_t = \dot{m}V_e + (p_e - p_a)A_e, \quad (42)$$

where f_t is the vehicle thrust and p_a is the atmospheric pressure. The launch vehicle being flexible in reality, the thrust follows the deformation of the vehicle at the point of application and hence known as the follower force.

We will consider a solid propellant rocket motor in a little more detail. The solid rocket motor is essentially a pressure vessel, with a nozzle at one end, partially filled with one or more blocks of solid propellant, called the grain, plus an ignition device as shown in figure 3. The combustion chamber itself stores the solid propellant and the propellant burns at its inner surface. The grain is fabricated to a configuration that produces a specific thrust which is time varying. Next, we consider the axial force distribution along the length of the vehicle.

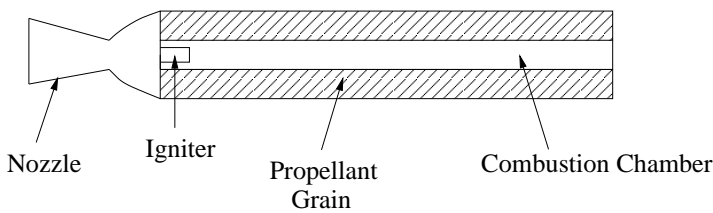


Figure 3: Cross section of a solid propellant rocket motor

3.3 Axial force on the vehicle

Stability is strongly influenced by the axial force distribution on the vehicle. For the purpose of representing the axial force distribution, a body fixed coordinate frame

is introduced with its origin at the nose tip of the vehicle. The distance of a material point on the vehicle axis, from the nose tip is denoted by x . The total axial force $P(x)$ is calculated by summing the aerodynamic and the inertia forces, that is,

$$\begin{aligned} P(x) &= f_s + f_x + (f_t - f_s - p_x l) \frac{x}{l}, \quad 0 < x < l_1, \\ &= f_s + f_x + (f_t - f_s - p_x l) \frac{x}{l} - p_c A_c, \quad l_1 < x < l, \end{aligned} \quad (43)$$

where p_x is the aerodynamic shear force per unit length of the vehicle, $f_x = \int_0^x p_x dx$ is the summation of the aerodynamic shear forces till distance x from the nose, $(f_t - f_s - p_x l) \frac{x}{l}$ is the summation of the inertia forces till x , A_c is the combustion chamber cross sectional area and l_1 is the distance from the nose to the front end of the solid propellant rocket motor as shown in figure 4.

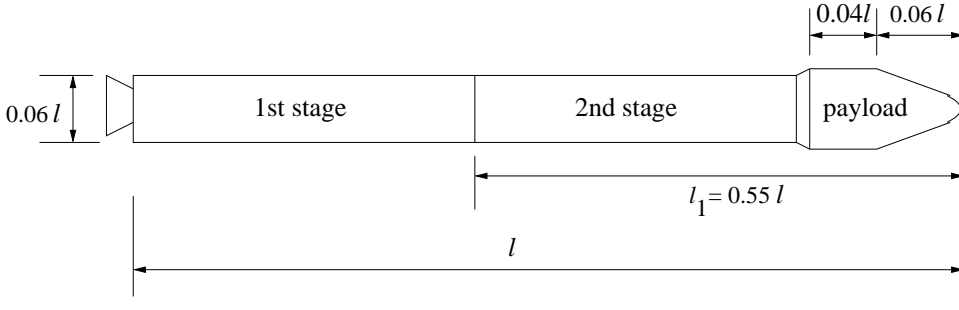


Figure 4: A two-stage vehicle configuration. The vehicle structure is discretized into 56 finite elements.

4 Finite Element Discretization

In this section, we turn our attention to the details regarding modelling and computation. To this end, the approach utilised is based on h - p finite element method. A vehicle segment of length l is discretized into m number of finite elements, each of length L as shown in figure 5. The transverse displacement $\mathbf{w}(x, t)$ within a finite element of length L is interpolated using polynomial of order $p \geq 3$ in x . This can be expressed as $\mathbf{w}(x, t) = \mathbf{N}(x) \mathbf{d}(t)$, where $\mathbf{d}(t) = \{w_1 \theta_1 w_2 \theta_2\}^T$ is the nodal displacement vector. $\mathbf{N}(x)$ is the shape function matrix, which is given by

$$\mathbf{N}(x) = \left[\begin{array}{cccc} \{1 - 3\xi^2 + 2\xi^3\} & \{\xi(\xi - 1)^2 L\} & \{3\xi^2 - 2\xi^3\} & \{\xi(\xi^2 - \xi)L\} \end{array} \right], \quad (44)$$

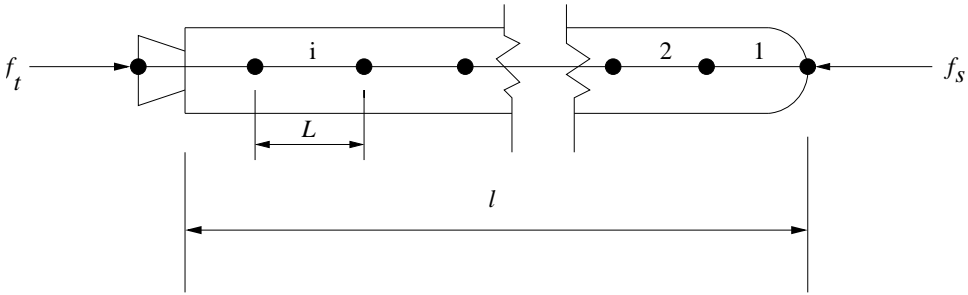


Figure 5: Vehicle segments discretized by finite elements. Finite element nodes are shown along the vehicle axis.

where $\xi = x/L \in [0, 1]$. The derivative of $\mathbf{N}(x)$ with respect to x is denoted by $\mathbf{N}'(x)$. The finite element matrices are derived using Lagrange's equation

$$\frac{\partial \mathcal{U}}{\partial \mathbf{q}} + \frac{d}{dt} \left(\frac{\partial \mathcal{T}}{\partial \dot{\mathbf{q}}} \right) - \frac{\partial \mathcal{T}}{\partial \mathbf{q}} - \frac{\partial \mathcal{W}_c}{\partial \mathbf{q}} = \mathbf{F}, \quad (45)$$

where \mathbf{q} is the generalised coordinate and \mathbf{F} includes the non-conservative forces. In this work, $\mathbf{d}(t)$ is considered as the generalised coordinate. An approach similar to that given by Rao (1996) is adopted to obtain the finite element matrices. The detailed derivations and expressions of all the finite element matrices are given in electronic supplementary material. In order to highlight the method for obtaining the finite element matrices, few finite element matrices are derived here.

4.1 Finite Element Stiffness Matrices

In order to obtain the finite element stiffness matrix, equation (13) is re-written with the help of $\mathbf{w}(x, t) = \mathbf{N}(x)\mathbf{d}(t)$ as

$$\mathcal{U} = \frac{1}{2} \int_I \int_A \sigma_{xx} \varepsilon_{xx} dA dx = \frac{1}{2} \int_I EI_2 \left(\frac{\partial^2 w}{\partial x^2} \right)^2 dx = \sum_{i=1}^m \frac{1}{2} EI_2 \int_0^L (\mathbf{d}^T \mathbf{N}''^T \mathbf{N}'' \mathbf{d}) dx,$$

and then in equation (45), one has

$$\frac{\partial \mathcal{U}}{\partial \mathbf{d}} = \sum_{i=1}^m \left[EI_2 \int_0^L \mathbf{N}''^T \mathbf{N}'' dx \right] \mathbf{d} = \sum_{i=1}^m \mathbf{K}_E \mathbf{d}, \quad (46)$$

where \mathbf{K}_E is the finite element stiffness matrix. \mathbf{K}_E is the conventional stiffness matrix corresponding to a stationary elastic beam (vehicle). Finite element stiffness

matrix due to axial velocity is determined from the kinetic energy term as follows:

$$\mathcal{T} = \frac{1}{2} \int_l \int_A \rho c_x^2 z^2 w_{,xx}^2 dA dx = \sum_{i=1}^m \frac{1}{2} \rho c_x^2 I_2 \int_0^L (\mathbf{d}^T \mathbf{N}''^T \mathbf{N}'' \mathbf{d}) dx ,$$

and in equation (45), one has

$$\frac{d}{dt} \left(\frac{\partial \mathcal{T}}{\partial \dot{\mathbf{d}}} \right) - \frac{\partial \mathcal{T}}{\partial \mathbf{d}} = - \sum_{i=1}^m \left[\rho c_x^2 I_2 \int_0^L \mathbf{N}''^T \mathbf{N}'' dx \right] \mathbf{d} = - \sum_{i=1}^m \mathbf{K}_I \mathbf{d} , \quad (47)$$

where $\mathbf{K}_I(c_x)$ is the finite element stiffness matrix due to axial velocity. In a similar way, a second finite element stiffness matrix due to axial velocity denoted as $\mathbf{K}_A(c_x)$ is also obtained. $\mathbf{K}_I(c_x)$ and $\mathbf{K}_A(c_x)$ are contributions due to the elasticity (curvature effects) of a moving vehicle. It is observed that the axial velocity contributes in reducing the overall bending stiffness of the vehicle and this effect is similar to that produced by a compressive axial load acting on the vehicle.

4.2 Finite Element Mass Matrices

The finite element translational mass matrix \mathbf{M}_T and the finite element mass matrix due to rotary inertia \mathbf{M}_R are obtained as

$$\mathbf{M}_T = \rho A \int_0^L \mathbf{N}^T \mathbf{N} dx , \quad \mathbf{M}_R = \rho I_2 \int_0^L \mathbf{N}'^T \mathbf{N}' dx . \quad (48)$$

4.3 Finite Element Damping Matrices

The finite element damping matrix is obtained from the kinetic energy term as

$$\mathcal{T} = \frac{1}{2} \int_l \int_A 2\rho c_x \dot{w} w_{,x} dA dx = \rho c_x \int_l \int_A (\dot{\mathbf{d}}^T \mathbf{N}^T \mathbf{N}' \mathbf{d}) dA dx ,$$

and in equation (45), one has

$$\frac{d}{dt} \left(\frac{\partial \mathcal{T}}{\partial \dot{\mathbf{d}}} \right) - \frac{\partial \mathcal{T}}{\partial \mathbf{d}} = \sum_{i=1}^m \left[\rho A c_x \int_0^L (\mathbf{N}^T \mathbf{N}' - \mathbf{N}'^T \mathbf{N}) dx \right] \dot{\mathbf{d}} = \sum_{i=1}^m \mathbf{C}_1 \dot{\mathbf{d}} , \quad (49)$$

where $\mathbf{C}_1(c_x)$ is the finite element damping matrix due to axial velocity. Similarly, a second finite element damping matrix due to axial velocity denoted as $\mathbf{C}_2(c_x)$ is obtained as

$$\mathbf{C}_2 = \rho I_2 c_x \int_0^L (\mathbf{N}'^T \mathbf{N}'' - \mathbf{N}''^T \mathbf{N}') dx . \quad (50)$$

It is observed that the axial velocity introduces equivalent damping in the system. The flow-induced damping has been observed previously in basic axial flow systems. The effect of this equivalent damping is similar to gyroscopic effects in a rotating system. The damping matrices are skew-symmetric matrices. It is this damping that causes the dynamic instability as the vehicle velocity is varied as a parameter. The details of the remaining finite element matrices are given in electronic supplementary material.

4.4 Finite Element System Assembly

The global mass matrix \mathbf{M}_G , the global stiffness matrix \mathbf{K}_G and the global damping matrix \mathbf{C}_G are obtained by assembling the respective element matrices over the entire vehicle structure. The global matrices are obtained as given below. The functional dependence of the finite element matrices on the parameters $(c_x, \dot{c}_x, \alpha, f_t, f_s, p_x)$ is also shown.

$$\mathbf{M}_G = \bigcup_m [\mathbf{M}_T + \mathbf{M}_R] , \quad (51)$$

$$\begin{aligned} \mathbf{K}_G = \bigcup_m & [\mathbf{K}_E - \mathbf{K}_I(c_x) - \mathbf{K}_A(c_x) + \mathbf{K}_{AR}(c_x, \alpha) - \mathbf{K}_{w1}(f_t, f_s, p_x) \\ & - \mathbf{K}_{w2}(f_t, f_s, p_x) + \mathbf{K}_{a1}(c_x, \dot{c}_x) + \mathbf{K}_{a2}(c_x, \dot{c}_x)] + \mathbf{K}_{nc1}(f_t) + \mathbf{K}_{nc2}(f_s) , \end{aligned} \quad (52)$$

$$\mathbf{C}_G = \bigcup_m [\mathbf{C}_1(c_x) + \mathbf{C}_2(c_x) - \mathbf{C}_{AR}(c_x, \alpha) + \mathbf{C}_{\rho1} + \mathbf{C}_{\rho2}] . \quad (53)$$

where m is the total number of finite elements. The matrices \mathbf{K}_{w1} and \mathbf{K}_{w2} are contributions to the stiffness due to the axial force and these reduce the bending stiffness of the system. The matrix \mathbf{K}_{nc1} is the stiffness matrix due to the non-conservative follower force f_t and \mathbf{K}_{nc2} is the stiffness matrix due to the non-conservative drag force f_s at the nose region. The matrices $\mathbf{K}_{AR}(c_x, \alpha)$ and $\mathbf{C}_{AR}(c_x, \alpha)$ are due to the contribution of aerodynamic forces. The matrices \mathbf{K}_{a1} and \mathbf{K}_{a2} are the stiffness matrices due to rate of change of momentum of the vehicle. The matrices $\mathbf{C}_{\rho1}$ and $\mathbf{C}_{\rho2}$ are the finite element damping matrices due to variable mass of the vehicle. The finite element matrices $\mathbf{K}_I(c_x)$, $\mathbf{K}_A(c_x)$, $\mathbf{K}_{a1}(c_x, \dot{c}_x)$, $\mathbf{K}_{a2}(c_x, \dot{c}_x)$, $\mathbf{C}_1(c_x)$ and $\mathbf{C}_2(c_x)$ are due to the contribution of velocity induced curvature effects. The velocity of the vehicle contributes to two effects namely velocity induced curvature effects and the aerodynamic effects (which are function of the velocity). The velocity induced curvature effects can be neglected at low speeds, but at higher speeds, these have significant effect on the dynamic characteristics of the vehicle. The system equations can now be written in a compact form as

$$\mathbf{M}_G \ddot{\mathbf{d}} + \mathbf{C}_G \dot{\mathbf{d}} + \mathbf{K}_G \mathbf{d} = \mathbf{0} . \quad (54)$$

4.5 Eigenvalue Problem

Equation (54) is transformed to first order state space form as follows:

$$\mathbf{X} = \begin{Bmatrix} \mathbf{d} \\ \dot{\mathbf{d}} \end{Bmatrix}, \quad \dot{\mathbf{X}} = \begin{Bmatrix} \dot{\mathbf{d}} \\ \ddot{\mathbf{d}} \end{Bmatrix} = \mathbf{A}\mathbf{X}, \quad (55)$$

where

$$\mathbf{A} = \begin{bmatrix} \mathbf{0} & \mathbf{I} \\ -\mathbf{M}_G^{-1}\mathbf{K}_G & -\mathbf{M}_G^{-1}\mathbf{C}_G \end{bmatrix}. \quad (56)$$

The eigenvalues λ for the system can be found by transforming the system to a standard eigenvalue problem

$$\mathbf{A}\mathbf{X} = \lambda\mathbf{X}, \quad (57)$$

where λ is generally complex, $\lambda = \sigma + i\omega$ with σ and ω being real numbers. The notion of stability is defined such that

- (1) the system is stable if $\sigma \leq 0$
- (2) the system undergoes dynamic instability (flutter) if $\sigma > 0$, $\omega \neq 0$
- (3) the system undergoes static instability (divergence) if $\sigma > 0$, $\omega = 0$

Alternatively, the eigenvalues and the eigenvectors of the system can be found by transforming equation (54) to a polynomial eigenvalue problem (PEP) as

$$[\mathbf{K}_G + \lambda\mathbf{C}_G + \lambda^2\mathbf{M}_G]\Psi = 0. \quad (58)$$

PEP is solved using standard MATLAB[®] routines, which gives the vector of eigenvalues λ_j and the corresponding eigenvector Ψ_j . The mode shape associated with a stable/ unstable mode is analysed by plotting Ψ_j over the span of the vehicle.

5 Numerical Simulations

Numerical simulations are carried out to determine the unstable regimes for a slender launch vehicle. Stability is determined in a quasi-static manner, that is, the eigenvalues of the system are determined at a specific instant of time, for a given vehicle thrust and speed. This analysis tells us, how the system behaviour will evolve for certain trajectory parameters and it gives information about the regimes in which the vehicle is likely to experience instability. Such information is important for mission planning and design of trajectory. Knowledge of vehicle unstable regimes is also an important input for control system design.

In this section, first, the present model is validated with those reported in published literature (Sundararamaiah & Johns 1976) for a special case of end thrust as a parameter. Next, the stability of a representative vehicle is investigated under the action of end thrust as a parameter, at a given velocity. Subsequently, the stability of a two-stage vehicle is determined for velocity as a parameter at constant maximum thrust, considering the mass variation of the vehicle. To study the velocity induced curvature effects, an order of magnitude analysis of finite element matrix terms is carried out. Next, the effect of combustion chamber pressure on the stability of the vehicle is considered. In the end, there is a discussion on the rigid body modes and the flexible modes of a vehicle. For the simulations, the vehicle is assumed to be moving at zero angle of attack ($\alpha = 0$) and zero angular velocity ($\Omega = 0$). Most of the launch vehicle structures are axially symmetric. Hence, it is reasonable to assume the vehicle mass to be symmetrical about the vehicle axis; that is, $I_1=0$. The propellant consumption leads to a decrease in the vehicle mass and a corresponding increase in the vehicle acceleration. The velocity at time t is calculated from

$$c_x(t) = \int_0^t \dot{c}_x dt, \quad \dot{c}_x(t) = \frac{(f_t - f_s - p_x l)}{M(t)}. \quad (59)$$

The stability is analysed based on the characteristics of eigenvalues and eigenvectors. It is convenient to deal with non-dimensional quantities. For this purpose, the thrust and the eigenvalues are non-dimensionalised by introducing the following parameters:

$$Q = \pi^2 f_t / P_{cr}, \quad P_{cr} = \pi^2 EI_2 / l^2, \quad \lambda \leftarrow \lambda \left(\frac{\rho A l^4}{EI_2} \right)^{1/2}. \quad (60)$$

Here P_{cr} is the Euler buckling load for a hinged-hinged beam-column of same length as the vehicle.

5.1 Numerical Validation of the Finite Element Simulation Results

From the published literature (e.g., Wu 1975, 1976), it was found that the finite element model of a flexible vehicle had been developed, including the effects of propulsive thrust. However, the velocity induced curvature effects were not included in these published research. Hence, our new results regarding velocity induced effects can not be validated with the published results. However, from the literature, results due to the propulsive end thrust are available. Hence, our computational results based on the developed finite element model is validated for end thrust as a parameter, by comparing the results reported by Sundararamaiah & Johns (1976). For the purpose of comparison, the velocity induced curvature effects

and the effect of aerodynamic forces are neglected. As an example, a representative vehicle data is taken. The length (l) of the vehicle is 40 m, flexural rigidity (EI_2) is 1.36×10^{10} N-m², mass per unit length (ρA) is 546 kg/m and maximum thrust developed (f_t) is 5000 kN. The h - p finite element model and standard eigenvalue routines are used for numerical simulations. The vehicle is discretized into 50 finite elements. The comparisons are shown in table 1. Here Q is the non-dimensional thrust. The results are in good agreement. The eigenvalues λ_3 and λ_4 are in fact the first two bending natural frequencies of the vehicle and these are obtained from the present model as imaginary numbers as shown in the table 1, indicating their oscillatory contribution in the time response of the vehicle. It is observed that natural frequencies decrease with the increase in the end thrust (same observation was reported by Sundararamaiah & Johns). At a critical thrust value ($Q/\pi^2 = 11.11$) that corresponds to $f_t = 9.37 \times 10^5$ kN, the two bending modes merge to a coupled mode. The eigenvalue corresponding to the coupled mode has a positive real part and a non-zero imaginary part indicating dynamic instability (flutter). This type of flutter is known as coupled mode flutter. For the representative vehicle, the critical thrust value is very high compared to its maximum thrust ($f_t = 5 \times 10^3$ kN).

The system under the action of propulsive thrust behaves in a similar manner to a vertical cantilevered beam-column subjected to a sub-tangential force. In the study by Sugiyama, Katayama, Kiriya & Ryu (2000), a solid rocket motor was mounted to a vertical cantilevered column at its tip end. Rocket thrust of the motor produces a tangential/ non-conservative force, while the self-weight of the motor a vertical/ conservative force. Thus, the combined action of the rocket thrust and the self-weight of the rocket motor produces a sub-tangential force. It is observed that the natural frequencies of the first two bending modes decreases to zero, with the increase in the compressive force, when only the conservative vertical force (self-weight) is applied. Hence the system loses its stability by divergence (buckling) and the corresponding load is known as buckling (divergence) load. When the rocket thrust (follower force) and the self-weight of the rocket motor are acting together, the system loses its stability by flutter. The flutter occurs when the two bending modes merge to a coupled mode. This happens at a higher compressive load as compared to the first buckling (divergence) load. So, in effect the follower force has a stabilising effect on the system.

5.2 Effect of propulsive thrust on the stability

Stability of the vehicle is investigated under the action of end thrust as a parameter, at a given velocity. The vehicle mass is assumed to be constant and the effect of aerodynamic forces is neglected. The stability property is investigated at $c = 500$ m/s ($M_\infty=1.47$) with the velocity induced curvature effects included. The first four

Table 1: Four smallest eigenvalues for constant thrust neglecting the velocity induced curvature effects. Q is the non-dimensional thrust and $i = \sqrt{-1}$

Q/π^2	λ_1	λ_2	λ_3	λ_4	Remarks
0.00	0.0	0.0	22.373 i	61.673 i	Present work
	0.0	0.0	22.3744	61.6958	(Sundararamaiah & Johns 1976)
	0.0	0.0	22.3733	61.6728	Exact
1.00	0.0	0.0	20.992 i	59.791 i	Present work
	0.0	0.0	20.99	59.82	(Sundararamaiah & Johns 1976)
2.00	0.0	0.0	19.565 i	57.826 i	Present work
	0.0	0.0	19.57	57.85	(Sundararamaiah & Johns 1976)
5.00	0.0	0.0	15.114 i	51.261 i	Present work
	0.0	0.0	15.13	51.30	(Sundararamaiah & Johns 1976)
11.126	0.0	0.0	1.48+23.078 i	-1.48+23.078 i	Present work
	0.0	0.0	23.10	23.10	(Sundararamaiah & Johns 1976)

non-zero eigenvalues with thrust as the parameter are shown in figure 6. As the non-dimensional thrust (Q/π^2) increases, an eigenvalue with a positive real part and a non-zero imaginary part is observed indicating dynamic instability (flutter). The divergence mode is observed from $Q/\pi^2 = 4.0$ to the range of thrust values considered (upto $Q/\pi^2 = 12$). It is observed that at $Q/\pi^2 = 5$, the divergence and the flutter modes crossover. For comparison, the bending modes neglecting the velocity induced effects are also shown in the figure. The finite element matrices \mathbf{K}_I , \mathbf{K}_A , \mathbf{K}_{a1} , \mathbf{K}_{a2} , \mathbf{C}_1 , \mathbf{C}_2 , \mathbf{K}_{AR} , \mathbf{K}_{nc2} and \mathbf{C}_{AR} are zero when velocity induced effects are neglected ($c_x, \dot{c}_x = 0$). When the velocity effects are included, the bending modes do not merge to a coupled mode for the range of thrust values considered (upto $Q/\pi^2 = 12$). This is unlike the bending modes which merge to a coupled mode (flutter mode) at $Q/\pi^2 = 11.11$ when velocity effects are neglected. The plots of bending modes neglecting the velocity induced curvature effects are in fact the plots of eigenvalues (λ_3 and λ_4 corresponding to present work) presented in table 1. When the velocity induced curvature effects are included, the instabilities are observed at lower thrust values. It is to be noted that the maximum thrust of the vehicle is $f_t = 5000$ kN that corresponds to a very low value of non-dimensional thrust ($Q/\pi^2 = 0.06$).

Next, we compare the results at low Mach number with the results from previous models (Wu 1975, 1976). The results from previous models are obtained by neglecting the velocity induced curvature effects ($M_\infty=0$). A plot of eigenvalues for thrust as a parameter at a lower Mach number ($M_\infty=0.25$) are shown in figure 7. For

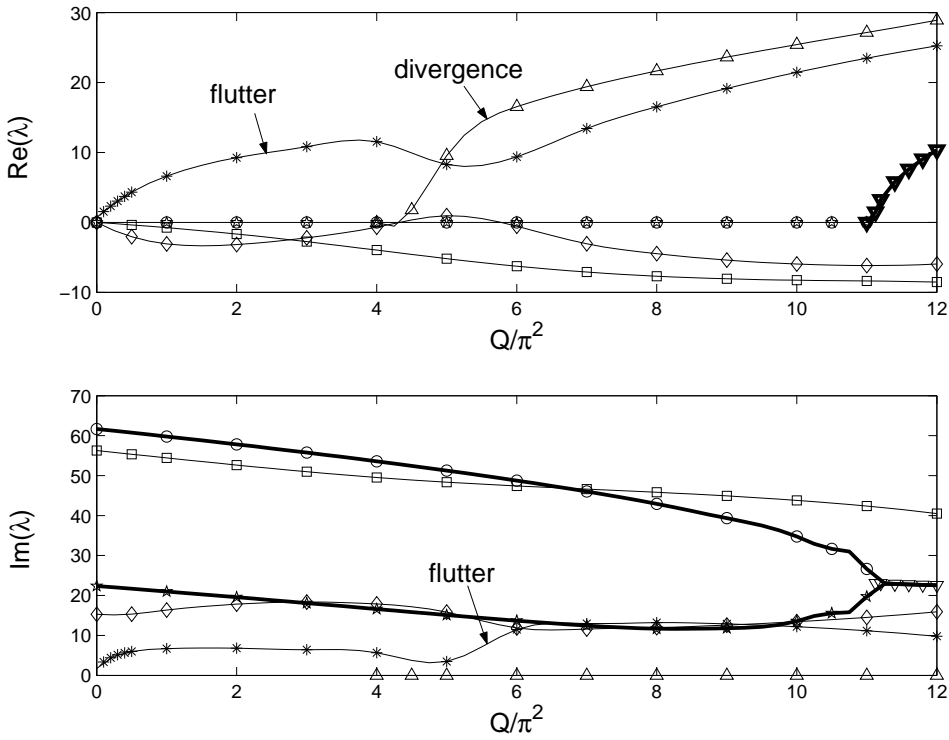


Figure 6: Eigenvalues for thrust as a parameter showing the velocity induced curvature effects, * flutter mode $c=500$ m/s ($M_\infty=1.47$), \diamond 1st bending mode $c=500$ m/s, \square 2nd bending mode $c=500$ m/s, \triangle divergence mode $c=500$ m/s, ∇ flutter mode neglecting velocity induced effects, \star 1st bending mode neglecting velocity induced effects, \circ 2nd bending mode neglecting velocity induced effects. $\dot{c}_x = f_t/M$, where M is the lift-off mass of the vehicle.

comparison, the first four modes neglecting the velocity induced effects ($M_\infty=0$) are also shown in the figure. It is observed that eigenvalue for mode 1 has a small positive real part at $M_\infty=0.25$. The real part of the eigenvalues for all the four modes are zero, when the velocity induced effects are neglected. Eigenvalues for mode 3 and mode 4 (which are the first two bending modes) match closely for $M_\infty=0.25$ and $M_\infty=0$. Hence, the results at low Mach number match closely with the results obtained from earlier models.

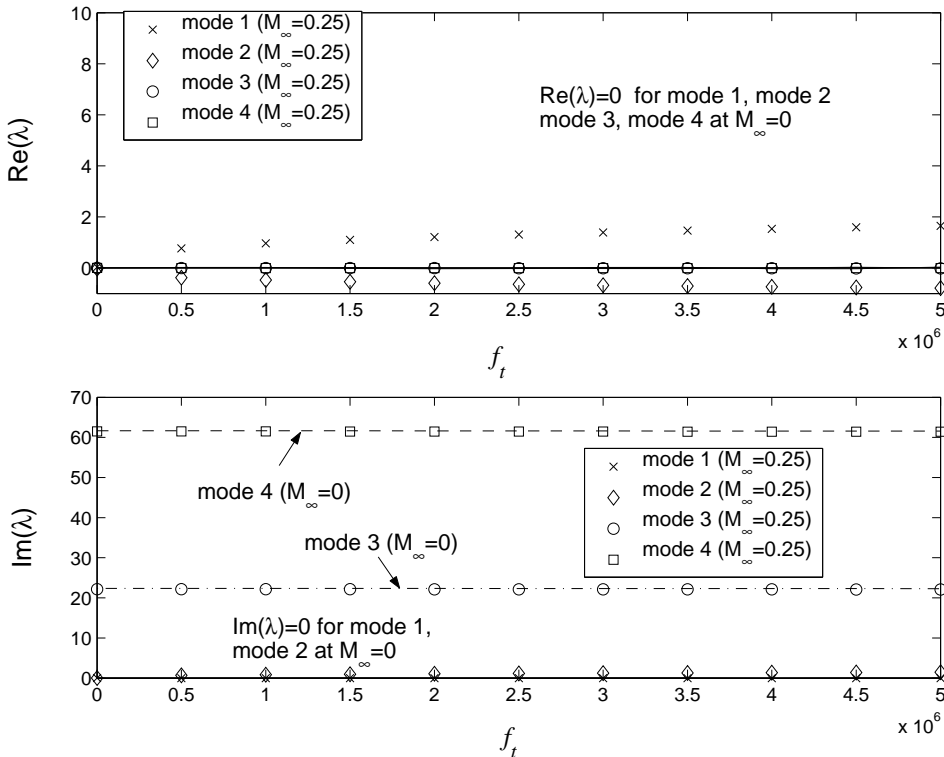


Figure 7: Eigenvalues for thrust (f_t) as a parameter at $M_\infty=0.25$. $\dot{c}_x = f_t/M$, where M is the lift-off mass of the vehicle.

5.3 Effect of velocity on the stability

Stability of the vehicle is analysed for velocity (free stream Mach number) as a parameter, at maximum propulsive thrust. Stability of the vehicle is dependent on the main trajectory parameters such as velocity and acceleration (thrust) profile, maximum dynamic pressure and angle of attack during flight. The information about stable regimes is useful for designing trajectories, that is, those trajectories can be selected on which the vehicle is stable for most of the operating regime. Numerical simulations are carried out for a two-stage vehicle configuration shown in figure 4. The data for the vehicle is given in table 2. The vehicle comprises of a conical nose region and two stages. The first stage is a solid propellant rocket motor with a nozzle at the end. The nose region consists of a uniform cross-section segment and a conical segment. The uniform cross-section segment accommodates the payload.

The conical segment is represented by four equivalent uniform cross-section segments. The number of finite elements used for each stage (segment) are also given in the table. For the numerical simulations, energy dissipated by the system due to material damping and due to friction in the joints is assumed to be 5% of the total strain energy. The first six non-zero eigenvalues with free stream Mach number ($M_\infty = c_x/c_o$) as a parameter upto $M_\infty=1.5$ are shown in figure 8. c_x obtained from equation (59) is used for obtaining \mathbf{K}_{a1} and \mathbf{K}_{a2} matrices. With the increase in the Mach number, branching (splitting) and merging of the modes is observed. At low Mach numbers, dynamic instability (flutter) occurs in mode 2. At $M_\infty=0.62$, the flutter mode splits into two divergence modes (mode 2a and 2b in the figure). The real part of the eigenvalue corresponding to one of the divergence modes (mode 2b) decreases and becomes zero at $M_\infty=0.87$. The eigenvalue corresponding to mode 3 is close to zero at low Mach numbers. At $M_\infty=0.91$, mode 2b and mode 3 merge to a coupled mode (denoted as mode 4 in the figure). As the Mach number increases, flutter occurs in mode 5 from $M_\infty=1.03$ to $M_\infty=1.65$. The imaginary part of the eigenvalues corresponding to modes 4 and 5 are very close from $M_\infty=1.03$ to $M_\infty=1.5$. As the Mach number increases, the imaginary part of the eigenvalues (natural frequencies) corresponding to modes 5 and 6 decreases. For the stationary free-free vehicle ($M_\infty=0$), modes 5 and 6 are the first two bending modes of the vehicle.

The first six non-zero eigenvalues with free stream Mach number as a parameter from $M_\infty=1.5$ to $M_\infty=3.0$ are shown in figure 9. As the Mach number increases from $M_\infty=1.5$, divergence and flutter are observed in different modes simultaneously. Divergence occurs in mode 2a from $M_\infty=1.50$ to $M_\infty=2.40$. Dynamic instability (flutter) occurs in mode 4 from $M_\infty=1.70$ to $M_\infty=2.37$. Since the real part of eigenvalue for mode 4 changes from negative to positive at $M_\infty=1.70$, this flutter is known as a single mode flutter (Hopf bifurcation). At $M_\infty=1.70$, mode 5 splits into two modes (denoted as mode 5a and 5b in the figure) having negative real part and zero imaginary part. At $M_\infty=2.31$, mode 5a and 5b merge to a coupled mode (denoted as mode 5c in the figure). From $M_\infty=2.36$ to $M_\infty=3.0$, mode 5c is a flutter mode (single mode flutter). Flutter (single mode flutter) occurs in mode 6 from $M_\infty=2.60$ to $M_\infty=3.0$. The real part of the eigenvalues for the divergence and flutter modes has higher magnitude at higher Mach numbers. This implies that the response (deformation) grows at a faster rate and leads to instability.

Prediction of unstable modes at high supersonic speeds using linear analysis is not fully reliable and non-linear analysis is required to predict the instabilities accurately. Large amplitude vibration and unsteady aerodynamics contribute to non-linearities in the system. After the onset of instability (divergence or flutter), higher amplitude of vibration start. As the amplitude increases, the linear theory does not

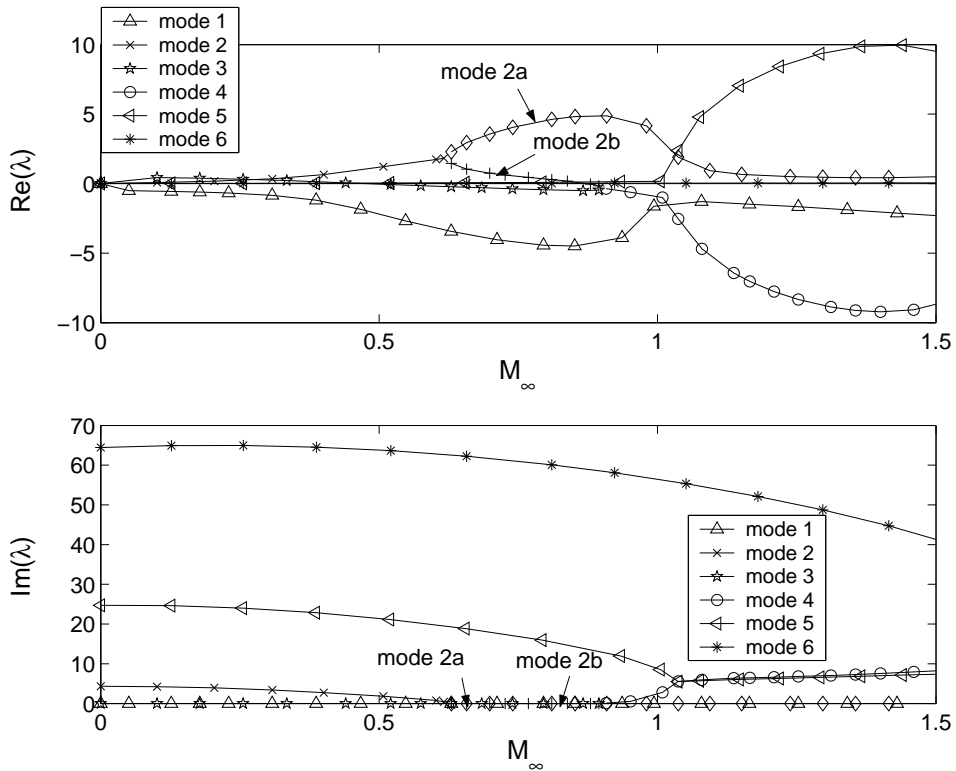


Figure 8: Eigenvalues (λ) for Mach Number (M_∞) as a parameter upto $M_\infty=1.5$ at constant maximum thrust $f_i=5140$ kN and c_x obtained from equation (59).

hold good. Due to the non-linearities, the system may develop limit cycle oscillations and may not become unstable. The non-linearities in the system will be considered in a future work.

5.4 Order of magnitude analysis

To study the velocity induced curvature effects, an order of magnitude analysis of finite element matrix terms is carried out. The terms of the finite element matrices are compared for a specific Mach number ($M_\infty=3.0$) in non-dimensionalised form

$$\mathbf{K}(m,n) \leftarrow \frac{\mathbf{K}(m,n)}{\rho A c_o^2 / l}, \quad \mathbf{C}(m,n) \leftarrow \frac{\mathbf{C}(m,n)}{\rho A c_o}. \quad (61)$$

A comparison of the first non-zero element of finite element matrices is shown in table 3. The finite element matrices are computed for a finite element consid-

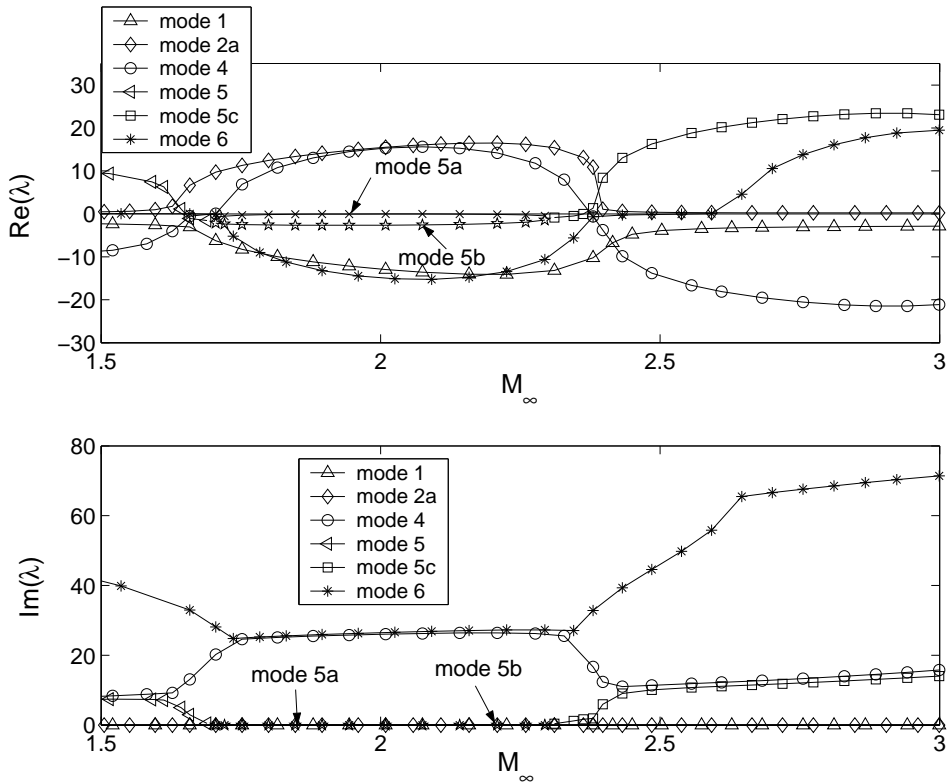


Figure 9: Eigenvalues (λ) for Mach Number (M_∞) as a parameter from $M_\infty=1.5$ to $M_\infty=3.0$ at constant maximum thrust $f_t=5140$ kN and \dot{c}_x obtained from equation (59).

ered in the first stage of the vehicle. The finite element matrices $\mathbf{K}_I(c_x)$, $\mathbf{K}_A(c_x)$, $\mathbf{K}_{a1}(c_x, \dot{c}_x)$, $\mathbf{K}_{a2}(c_x, \dot{c}_x)$, $\mathbf{C}_1(c_x)$ and $\mathbf{C}_2(c_x)$ are due to the contribution of velocity induced curvature effects. The terms of finite element matrices $\mathbf{K}_I(c_x)$ and $\mathbf{K}_A(c_x)$ are function of square of the velocity (c_x). The terms of $\mathbf{K}_I(c_x)$ and $\mathbf{K}_A(c_x)$ are one order of magnitude and two order of magnitude less, respectively, than the conventional finite element stiffness matrix \mathbf{K}_E terms. The terms of all other finite element stiffness matrices are significantly lower. The terms of finite element matrices due to aerodynamic forces are zero due to zero angle of attack. Also, the finite element is considered in the cylindrical segment of the vehicle where the aerodynamic lift force is zero. The terms of finite element damping matrices due to velocity $\mathbf{C}_1(c_x)$ and $\mathbf{C}_2(c_x)$ are significantly lower than the \mathbf{K}_E term, but this damping can desta-

Table 2: Data for a two-stage vehicle

Stage (Segment)	Segment Length/l	No. of elements	E/ρ (m^2s^{-2})	I_2/A (m^2)
1	0.45	25	2.564e7	0.9744
2	0.45	25	2.564e7	0.9744
Nose region	0.04	2	2.5e7	1.3039
Nose region	0.02	1	2.5e7	0.8008
Nose region	0.02	1	2.5e7	0.4202
Nose region	0.01	1	2.5e7	0.1875
Nose region	0.01	1	2.5e7	0.0625

bilise the system.

Table 3: Order of magnitude analysis of finite element matrix terms for $M_\infty=3.0$

$\mathbf{K}_E(1,1)$	$\mathbf{K}_I(1,1)$	$\mathbf{K}_A(1,1)$	$\mathbf{K}_{w1}(1,1)$	$\mathbf{K}_{w2}(1,1)$	$\mathbf{K}_{nc1}(4,3)$
2.27e5	9514.9	2908.5	0.048	2.93	3.65
$\mathbf{K}_{a1}(1,2)$	$\mathbf{K}_{a2}(1,1)$	$\mathbf{K}_{AR}(1,1)$	$\mathbf{C}_1(1,2)$	$\mathbf{C}_2(1,2)$	$\mathbf{C}_{AR}(1,1)$
0.03	0.01	0.0	0.05	0.808	0.0

5.5 Effect of combustion chamber pressure on the stability

The change in combustion chamber pressure changes the exhaust velocity and the mass flow rate. Consequently, the propulsive thrust also gets changed since it is a function of the mass flow rate and the exhaust velocity. The chamber pressure also affects the axial force distribution on the vehicle. Three of the first six eigenvalues with Mach number as a parameter at constant chamber pressure ($p_o=7$ MPa) and for varying chamber pressure are shown in figure 10. The chamber pressure varies with time and since Mach number also varies with time, the variation of the chamber pressure with the Mach number is shown in the inset of the figure 10. It is observed that the real part of the eigenvalue for the divergence and the flutter modes is higher for varying chamber pressure when the chamber pressure is $1.5p_o$. Also the imaginary part of the eigenvalue (frequency) for mode 5 is higher for varying chamber pressure.

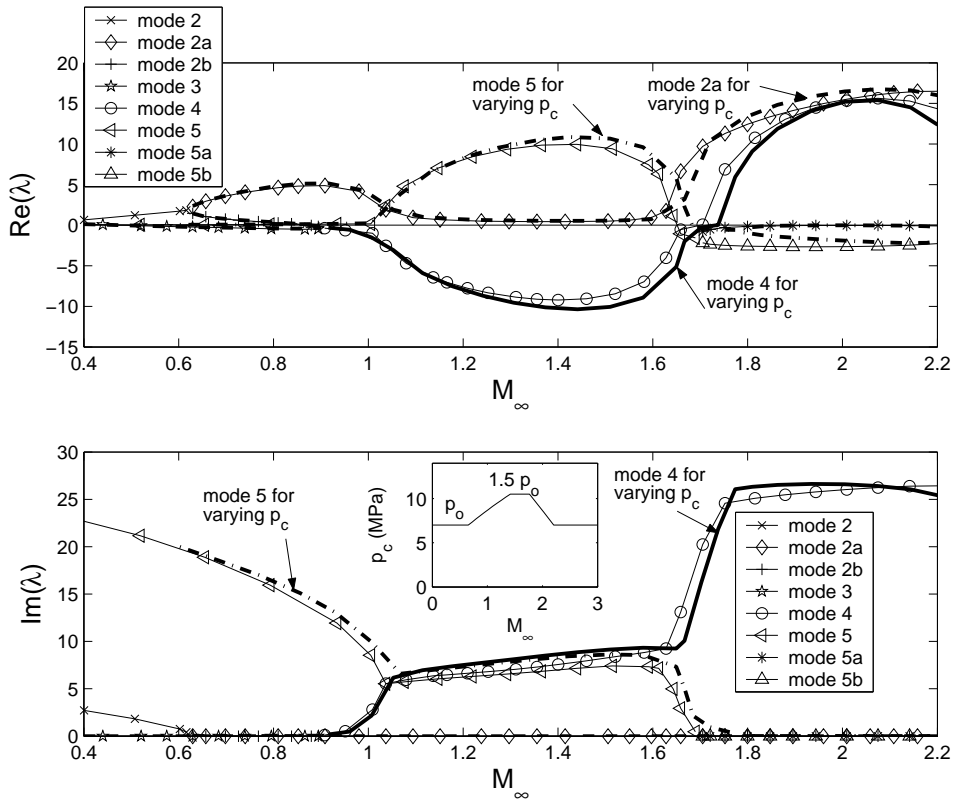


Figure 10: Eigenvalues (λ) for Mach Number (M_∞) as a parameter at constant chamber pressure ($p_0 = 7$ MPa) and for varying chamber pressure. The branches shown by arrow are for varying pressure (profile of p_c Vs. M_∞ is shown in the inset) and the other branches are for constant pressure. \dot{c}_x is obtained from equation (59).

5.6 Discussion on Rigid Body Modes and Flexible Modes

There are two types of rigid body modes ($\lambda = 0$) for a free-free beam, which correspond to rigid body translations and rigid body rotations. Moving flexible vehicles are free-free unconstrained structures. In the context of moving flexible vehicles under the propulsive thrust (follower force) and aerodynamic forces, zero eigenvalues may not be obtained. The flexible modes of a moving flexible vehicle are not identical to the flexible modes of a stationary vehicle. The rigid body motion influences the flexible modes of the system. With the increase in velocity of the center of mass of the vehicle, the total kinetic energy of the system increases and

the energy of the vibrational modes also increases due to coupling between the rigid body motion and the flexible modes. Due to the higher energy of the vibrational modes, the system may not be able to store or dissipate the energy and the unstable modes are more likely to occur.

There are two external forces acting on the system: vehicle thrust and the aerodynamic forces. The vehicle is also subjected to forces which arise due to the curvature of the moving vehicle. All the above forces along with the elastic and inertia forces determine the behaviour of the system. The point to be noted is that the present analysis is carried out for unguided launch vehicles neglecting the control forces. The present day launch vehicles have sophisticated control and guidance systems which are responsible for accurate vehicle trajectory and reliable performance.

The present analysis shows that as the vehicle speed increases, the vehicle modes are distinctly different from that of a stationary vehicle. This implies change in the stress and the bending moment on the vehicle structure with the change in the vehicle speed, which needs to be taken care of in the design of a vehicle. There are certain important implications from design and flight control points of view. Any control system design should account for such a change in the eigenvalues and mode shapes. The placement of sensors and actuators in the vehicle also assumes significance in view of the changing mode shapes. Similar concern arises while considering large distributed payload and its placements.

6 Conclusions

A modelling approach toward the dynamic instability of slender space launch vehicles subjected to propulsive thrust and aerodynamic forces is presented. The new aspect of this work is the inclusion of velocity induced curvature effects that includes the Coriolis and centrifugal forces due to curvature of a moving flexible vehicle. The flexible body dynamics of the moving vehicle is studied in an inertial frame of reference within the variational framework. A one-dimensional model of the vehicle is developed by considering the coupling of the rigid body modes and the flexible modes. The model incorporates the aerodynamic forces and the thrust of the vehicle. A h - p finite element model is developed to solve the eigenvalue problem. Predictions regarding stability regimes for a vehicle subjected to the end thrust are validated. Stability of the vehicle is investigated under the action of end thrust as a parameter, at a given velocity. The results at low Mach number match closely with the results obtained from previous models published in the literature. Numerical simulations are carried out for a representative vehicle to determine the regions of instability with vehicle speed as a parameter upto $M_\infty=3.0$. With the increase in the Mach number, branching (splitting) and merging of the modes is

observed. At higher Mach numbers, divergence and flutter are observed in different modes simultaneously.

The eigenvalues and eigenvectors are in general complex for a given vehicle thrust and velocity. For moving flexible vehicles under the propulsive thrust and aerodynamic forces, zero eigenvalues may not be obtained, unlike a stationary free-free vehicle (beam) for which two types of rigid body modes exist ($\lambda=0$).

Literature review shows that for space launch vehicles, flexible body dynamics has been studied in body coordinate system due to which the influence of the rigid body motion on the flexible modes of the vehicle is neglected. As the numerical simulations show, the coupling of these two types of modes can change the dynamic characteristics of the vehicle completely. Understanding of related phenomena for future space missions is important.

Detailed analysis of the vehicle can be carried out by considering a more detailed model in terms of accurate mass and stiffness distributions. Understanding the effect of time-varying coefficients, angle of attack and the angular velocity in the model is an open area of research. Also non-linearities due to large amplitude vibration and unsteady aerodynamics can be considered in future. In the present work, empirical relations are used to obtain the aerodynamic coefficients. This research can be extended by considering a more detailed aerodynamics model. At present, the effect of combustion process is incorporated through the propulsive thrust and the variation of axial force in the vehicle. A more detailed combustion coupled model is under development to study the combustion induced instabilities in the vehicle.

References

Allen, H. J., Perkins, E. W. (1951): A Study of Effects of Viscosity on Flow over Slender Inclined Bodies of Revolution. NACA Report 1048, Washington.

Argyris, J. (1982): An excursion into large rotations. *Computer Methods in Applied Mechanics and Engineering* vol. 32, pp. 85–155.

Atluri, S. N. (1984): Alternate Stress and Conjugate Strain Measures, and Mixed Variational Formulations Involving Rigid Rotations, for Computational Analyses of Finitely Deformed Plates and Shells: Part-I: Thoery. *Computers & Structures*, Vol. 18, No. 1, pp. 93-116.

Atluri, S. N. (2005): *Methods of Computer Modeling in Engineering and the Sciences*. Tech Science Press.

Atluri, S. N., Cazzani A. (1994): Rotations in Computational Solid Mechanics, Feature Article. *Archives for Computational Methods in Engg.*, ICNME, Barcelona,

Spain, Vol 2, No 1, pp 49-138.

Atluri, S. N., Iura, M., Vasudevan, S. (2001): A consistent theory of finite stretches and finite rotations, in space-curved beams of arbitrary cross-section. *Computational Mechanics* **27(4)**, 271-281.

Atluri, S. N., Liu, H. T. and Han, Z. D. (2006a): Meshless Local Petrov-Galerkin (MLPG) Mixed Collocation Method For Elasticity Problems. *CMES: Computer Modeling in Engineering and Sciences* Vol. 14, No. 3, pp. 141-152.

Atluri, S. N., Liu, H. T. and Han, Z. D. (2006b): Meshless Local Petrov-Galerkin (MLPG) Mixed Finite Difference Method for Solid Mechanics. *CMES: Computer Modeling in Engineering and Sciences* Vol. 15, No. 1, pp. 1-16.

Bathe, K. J., Ramm, E., Wilson, E. L. (1975): Finite Element Formulations for large deformation dynamic analysis. *International Journal for Numerical Methods in Engineering*, Vol. 9, pp. 353–386.

Battini, J.-M. (2008): Large Rotations and Nodal Moments in Corotational Elements. *CMES: Computer Modeling in Engineering and Sciences* Vol. 33, No. 1, pp. 1–16.

Beal, T. R. (1965): Dynamic Stability of a Flexible Missile Under Constant and Pulsating Thrusts. *AIAA Journal* **3**, 486–495.

Belytschko, T., Hsieh, J. (1973): Non-Linear transient finite element analysis with convected coordinates. *International Journal for Numerical Methods in Engineering*, Vol. 7, pp. 255–271.

Bisplinghoff, R. L., Ashley, H. (1962): *Principles of Aeroelasticity*, Wiley, New York.

Bolotin, V. V., Grishko, A. A., Panov, M. Y. (2002): Effect of Damping on the Postcritical Behaviour of Autonomous Non-conservative Systems. *International Journal of Non-linear Mechanics* **37**, 1163–1179.

Bolotin, V. V. (1963): *Nonconservative Problems of the Theory of Elastic Stability*. English Translation: Pergamon Press, Oxford.

Capri, F., Mastroddi, F., Pizzicaroli, A. (2006): Linearized Aeroelastic Analysis for a Launch Vehicle in Transonic Flight Conditions. *Journal of Spacecraft and Rockets*, Vol. 43, No. 1, pp. 92-104.

Cornelisse, J. W., Schoyer, H. F. R., Wakker, K. F. (1979): *Rocket Propulsion and Spaceflight Dynamics*, pp. 320. London: Pitman Publishing Ltd.

Cui, X. Y., Liu, G. R., Li, G. Y., Zhao, X., Nguyen, T. T., Sun, G. Y. (2008): A Smoothed Finite Element Method (SFEM) for Linear and Geometrically Nonlinear Analysis of Plates and Shells. *CMES: Computer Modeling in Engineering and Sciences* Vol. 28, No. 2, pp. 109-126.

- Dotson, K. W., Baker, R. L., Sako, B. H.** (1998): Launch Vehicle Self Sustained Oscillation from Aeroelastic Coupling Part 1: Theory. *Journal of Spacecraft and Rockets*, Vol. 35, No. 3, pp. 365-373.
- Doyle, J. F.** (1997): *Wave Propagation in Structures: Spectral Analysis using Fast Discrete Fourier Transforms*, 2nd ed. New York: Springer-Verlag.
- Dugundji, J.** (1992): Nonlinear Problems of Aeroelasticity. *Computational Non-linear Mechanics in Aerospace Engineering*, edited by Atluri, Satya N., Progress in Astronautics and Aeronautics, AIAA, Washington DC, pp. 127.
- Elishakoff, I.** (2005): Controversy Associated With the So-Called "Follower Forces": Critical Overview. *Applied Mechanics Reviews* **58**, 117–142.
- Elyada, D.** (1989): Closed-Form Approach to Rocket-Vehicles Aeroelastic Divergence. *Journal of Spacecraft and Rockets*, Vol. 26, No. 2, pp. 95-102.
- Ericsson, L. E.** (1967): Aeroelastic Instability Caused by Slender Payloads. *Journal of Spacecraft and Rockets*, Vol. 4, No. 1, pp. 65-73.
- Ericsson, L. E., Reding J. P.** (1986): Fluid Dynamics of Unsteady Separated Flow. Part 1-Bodies of Revolution. *Progress in Aerospace Sciences*, Vol. 23, No. 1, pp. 1-84.
- Ericsson, L. E., Pavish, D.** (2000): Aeroelastic Vehicle Dynamics of a Proposed Delta II 7920-10L Launch Vehicle. *Journal of Spacecraft and Rockets*, Vol. 37, No. 1, pp. 28-38.
- Fabignon, Y., Dupays, J., Avalon, G., Vuillot, F., Lupoglazoff, N., Casalis, G., Prevost, M.** (2003): Instabilities and Pressure Oscillations in Solid Rocket Motors. *Aerospace Science and Technology* **7**, 191–200.
- Geradin, M., Cardona, A.** (1989): Kinematics and Dynamics of rigid and flexible mechanisms using finite elements and quaternion algebra. *Computational Mechanics* Vol. 4, pp. 115–136.
- Gopalakrishnan, S., Martin, M., Doyle J. F.** (1992): A Matrix Methodology for Spectral Analysis of Wave Propagation in Multiple Connected Timoshenko Beams. *Journal of Sound and Vibration*, Vol. 158, No. 1, pp. 11-24.
- Han, Z. D., Rajendran, A. M., Atluri, S. N.** (2005): Meshless Local Petrov-Galerkin (MLPG) Approaches for Solving Nonlinear Problems with Large Deformations and Rotations. *CMES: Computer Modeling in Engineering and Sciences* **10(1)**, pp. 1-12.
- Han, Z. D., Liu, H. T., Rajendran, A. M., Atluri, S. N.** (2006): The Applications of Meshless Local Petrov-Galerkin (MLPG) Approaches in High-Speed Impact, Penetration and Perforation Problems. *CMES: Computer Modeling in Engineering and Sciences* Vol. 14, No. 2, pp. 119-128.

Himmelblau, H., Manning, J. E., Piersol, A. G., Rubin, S. (2001): *Dynamic Environmental Criteria*. NASA Technical Handbook, NASA-HDBK-7005.

Hodges, D. H. (1990): A Mixed Variational Formulation Based on Exact Intrinsic Equations for Dynamics of Moving Beams. *International Journal of Solids and Structures* Vol. 26, No. 11, pp. 1253–1273.

Hodges, D. H., Pierce, G. A. (2002): *Introduction to Structural Dynamics and Aeroelasticity*. New York: Cambridge University Press.

Hsiao, K., Jang, J. (1991): Dynamic Analysis of Planar Flexible Mechanisms by Corotational Formulation. *Computer Methods in Applied Mechanics and Engineering* **87**, 1–14.

Humbad, N. G. (1978): Static Aeroelastic Analysis of Guided Slender Launch Vehicles. *Journal of Spacecraft and Rockets*, Vol. 15, No. 1, pp. 12-17.

Ijima, K., Obiya, H., Iguchi, S., Goto, S. (2003): Element Coordinates and the Utility in Large Displacement Analysis of a Space Frame. *CMES: Computer Modeling in Engineering and Sciences*, Vol. 4, No. 2, pp. 239-248.

Iura, M., Atluri, S. N. (1988a): Dynamic Analysis of Finitely Stretched and Rotated 3-D Space Curved Beams. *Computers & Structures* Vol. 29(5), pps. 875–889.

Iura, M., Atluri, S. N. (1988b): Nonlinearities in Dynamics & Control of Space Structures:-Some Issues for Computational Mechanics. *Large Space Structures:-Dynamics and control* S.N. Atluri, A.K. Amos, Eds., Springer-Verlag, Berlin, Chapter 3.

Iura, M., Atluri, S. N. (1989): On a Consistent Theory and Variational Formulation, of Finitely Stretched and Rotated 3-D Space-Curved Beams. *Computational Mechanics* Vol. 4(1), pp. 73–88.

Iura, M., Atluri, S. N. (1995): Dynamic Analysis of Planar Flexible Beams with Finite Rotations by Using Inertial & Rotating Frames. *Computers & Structures* Vol. 55, No. 3, pp. 453–462.

Iura, M., Atluri, S. N. (2003): Advances in Finite Rotations in Structural Mechanics. *CMES: Computer Modeling in Engineering and Sciences*, Vol. 4, No. 2, pp. 213-216.

Iura, M., Suiteake, Y., Atluri, S. N. (2003): Accuracy of co-rotational formulation for 3-D Timoshenko's beam. *CMES: Computer Modeling in Engineering and Sciences*, Vol.4, No. 2, pp. 249–258.

Ivanov, A.P. (2001): The Stability of Mechanical Systems Subjected to Impulsive Actions. *Journal of Applied Mathematics and Mechanics*, Vol. 65, No. 4, pp. 617–629.

Jones, N., Wierzbicki, T. (1987): Dynamic Plastic Failure of a Free-Free Beam.

International Journal of Impact Engineering **6**, 3, 225–240.

Jorgensen, L. H. (1973): Prediction of Static Aerodynamic Characteristics for Space- Shuttle-Like and Other Bodies at Angles of Attack from 0° to 180° . NASA TN D-6996, Washington.

Kane, T. R., Levinson, D. A. (1981): Simulation of large motions of non-uniform beams in orbit: Part II–The Unrestrained Beam. *The Journal of the Astronautical Sciences* Vol. 29, No. 3, pp. 213–244.

Kulikov, G. M., Plotnikova, S. V. (2008): Finite Rotation Geometrically Exact Four-Node Solid-Shell Element with Seven Displacement Degrees of Freedom. *CMES: Computer Modeling in Engineering and Sciences* Vol. 28, No. 1, pp. 15–38.

Lee, K., Wu, C. T., Clarke, G. V., Lee, S. W. (2008): Computational Modeling of a Lightweight Composite Space Reflector using Geometrically Nonlinear Solid Shell Elements. *CMES: Computer Modeling in Engineering and Sciences* Vol. 33, No. 1, pp. 109–130.

Lesaffre, N., Sinou, J-J., Thouverez, F. (2007): Stability Analysis of Beams Rotating on an Elastic Ring Application to Turbo machinery Rotor-Stator Contacts. *International Conference on Computational & Experimental Engineering and Sciences* Vol.2, No.4, pp.101-110.

Lin, C. C. (1997): Stability and Vibration Characteristics of Axially moving plates. *International Journal of Solids and Structures* **34**, 24, 3179–3190.

Lin, S. M., Lee, S. Y., Lin Y. S. (2008): Modeling and Bending Vibration of the Blade of a Horizontal-Axis Wind Power Turbine. *CMES: Computer Modeling in Engineering and Sciences* Vol. 23, No. 2, pp. 175–186.

Liu, C.-S. (2006): The computations of large rotation through an index two nilpotent equation. *CMES: Computer Modeling in Engineering and Sciences* Vol. 16, No. 3, pp. 157–176.

Majorana, C. E., Salomoni, V. A. (2008): Dynamic Nonlinear Material Behaviour of Thin Shells in Finite Displacements and Rotations. *CMES: Computer Modeling in Engineering and Sciences* Vol. 33, No. 1, pp. 49–84.

Meirovitch, L., Wesley, D. A. (1967): On the Dynamic Characteristics of a Variable Mass Slender Elastic Body under High Accelerations. *AIAA Journal* **5**, 8, 1439–1447.

Mitra, M., Gopalakrishnan S. (2006): Wavelet Based 2-D Spectral Finite Element Formulation for Wave Propagation Analysis in Isotropic Plates. *CMES: Computer Modeling in Engineering and Sciences* Vol. 15, No. 1, pp. 49–68.

Murphy, C. H., Mermagen, W. H. (2003): Flight Motion of a Continuously Elas-

- tic Finned Missile. *Journal of Guidance, Control and Dynamics* **26**, 1, 89–98.
- NASA SP-8003** (1964): *Flutter, Buzz and Divergence*. NASA Space Vehicle Design Criteria (Structures).
- Okamoto, S., Omura Y.** (2003): Finite-Element Nonlinear Dynamics of Flexible Structures in Three Dimensions. *CMES: Computer Modeling in Engineering and Sciences*, Vol. 4, No. 2, pp. 287-300.
- Oppenheim, B. W., Rubin, S.** (1993): Advanced Pogo Stability Analysis for Liquid Rockets. *Journal of Spacecraft and Rockets*, Vol. 30, No. 3, pp. 360–373.
- Park, Y. P., Mote Jr., C. D.** (1985): The Maximum Controlled Follower Force on a Free-Free Beam Carrying a Concentrated Mass. *Journal of Sound and Vibration*, Vol. 98, No. 2, pp. 247-256.
- Platus, D. H.** (1992): Aeroelastic Stability of Slender Spinning Missiles. *Journal of Guidance, Control and Dynamics*, **15**, 1, 144-151.
- Quadrelli, B. M., Atluri, S. N.** (1996): Primal and Mixed Variational Principles for Dynamics of Spatial Beams. *AIAA Journal*, Vol. 34, pp. 2395-2405.
- Quadrelli, B. M., Atluri, S. N.** (1998): Analysis of Flexible Multibody Systems with Spatial Beams Using Mixed Variational Principles. *International Journal for Numerical Methods in Engineering*, Vol. 42, pp. 1071–1090.
- Rainey, L. B. (ed.)** (2004): *Space Modeling and Simulation: Roles and Applications throughout the System Life Cycle*. Space Technology Series, AIAA, pp. 350-356, Reston, Virginia, USA.
- Rao, J. S.** (1996): *Rotor Dynamics*. New Delhi: New Age International Limited.
- Rochinha, F. A., Sampaio, R.** (2000): Non-Linear Rigid Body Dynamics: Energy and Momentum Conserving Algorithm. *CMES: Computer Modeling in Engineering and Sciences* Vol. 1, No. 2, pp. 7–18.
- Shiau, L. C., Kuo S. Y.** (2007): Flutter of Thermally Buckled Composite Sandwich Plates. *CMC: Computers, Materials and Continua* Vol. 5, No. 3, pp. 213-222.
- Simo, J. C., Vu-Quoc, L.** (1986): On the Dynamics of Flexible Beams Under Large Overall Motions-The Plane Case:Part 1 and Part 2. *Journal of Applied Mechanics, Transactions of the ASME* **53**, pp. 849–863.
- Simo, J. C., Vu-Quoc, L.** (1988): On the dynamics of finite-strain rods undergoing large motions: a geometrically exact approach. *Computer Methods in Applied Mechanics and Engineering* **66(2)**, pp. 125–161.
- Sugiyama, Y., Katayama, K., Kiriya, K., Ryu, B. J.** (2000): Experimental Verification of Dynamic Stability of Vertical Cantilevered Columns Subjected to a Sub-Tangential Force. *Journal of Sound and Vibration* **236**, 2, 193–207.

Sundararamaiah, V., Johns, D. J. (1976): Comment on "On the Stability of a Free-Free Beam Under Axial Thrust Subjected to Directional Control. *Journal of Sound and Vibration* **48**, 4, 571–574.

Trikha, M., Mahapatra, D. R., Gopalakrishnan, S., Pandiyan R. (2008): Analysis of Aeroelastic Stability of a Slender Launch Vehicle using Aerodynamic Data. *46th AIAA Aerospace Sciences Meeting and Exhibit AIAA 2008-310*.

Trikha, M., Gopalakrishnan, S., Mahapatra, D. R., Pandiyan R. (2008): Influence of Combustion Coupled Follower Force and Mass Sensitivity on Launch Vehicle Stability. *49th AIAA/ASME/ASCE/AHS/ASC Structures, Structural Dynamics and Materials Conference AIAA 2008-2023*.

Vinod, K. G., Gopalakrishnan S., Ganguli R. (2006): Wave Propagation Characteristics of Rotating Uniform Euler-Bernoulli Beams. *CMES: Computer Modeling in Engineering and Sciences* Vol. 16, No. 3, pp. 197-208.

Wen, P. H., Hon, Y. C. (2007): Geometrically Nonlinear Analysis of Reissner-Mindlin Plate by Meshless Computation. *CMES: Computer Modeling in Engineering and Sciences* Vol. 21, No. 3, pp. 177-192.

Wickert, J. A., Mote Jr., C. D. (1988): Current Research on the Vibration and Stability of Axially Moving Materials. *The Shock and Vibration Digest* **20**, 5, 3–13.

Wickert, J. A., Mote Jr., C. D. (1990): Classical Vibration Analysis of Axially Moving Continua. *Journal of Applied Mechanics, Transactions of the ASME* **57**, 738–744.

Wong, S., Shie, Y. (2008): Large Deformation Analysis with Galerkin based Smoothed Particle Hydrodynamics. *CMES: Computer Modeling in Engineering and Sciences* Vol. 36, No. 2, pp. 97-118.

Wu, J. J. (1975): On the Stability of a Free-Free Beam Under Axial Thrust Subjected to Directional Control. *Journal of Sound and Vibration* **43**, 1, 42–52.

Wu, J. J. (1976): Missile Stability Using Finite Elements-an Unconstrained Variational Approach. *AIAA Journal* **14**, 3, 313–319.

Young Jr., C. P. (1968): Analysis of the Aeroelastic Divergence of Two Experimental Unguided Launch Vehicles. NASA TN D-4846, Washington.

